Exploring the (boundaries) of the Moving Boundary Problem

by

Claudia Olivia Hermans

Delft University of Technology
Delft, The Netherlands

Applied Mathematics and Applied Physics

Supervisors: Prof. dr. H.M. Schuttelaars
Prof. dr.ir. C.R. Kleijn

Abstract

The sea and the shoreline form a complex ecosystem driven by tides. So far, studies often ignore the moving boundary caused by these tides. The focus of this thesis to incorporate this boundary by using a coordinate transformation and a time-explicit numerical method. To achieve this, first the one-dimensional shallow water equations are derived from the 3D Navier Stokes equations. Then these 1D equations are non-dimensionalized and the coordinate transformation is done. This results in a system of non-linear equations. The seabed is modelled as a straight line. At the seaward side there is a periodic forced wave and at the landward side the water depth is 0. The time-explicit numerical method of Lax-Friedrichs is used. This method is stable under a more restricted Courant-Friedrichs-Lewy condition and is convergent for refined grids. For the Ameland inlet system the water depth, velocity and length of the basin results are calculated and compared to a simplified model and complemented by a Fourier analysis. The results are realistic (constant in the beginning of the basin with visible non-linearities at the landward side). An analysis is done to understand how the model behaves for different physical parameters, such as: the amplitude of the periodically forced wave, the undisturbed water depth, the length of the basin and the resistance. The model remains stable and the results are realistic.

Samenvatting voor vrienden en familie

In Ameland kan je wadlopen, dat betekent dat je tijdens eb een wandeling gaat maken door de Waddenzee. Tijdens vloed is dit niet handig. Het einde van de waterlijn verandert steeds. Deze bewegende rand heb ik toegevoegd aan een water model. Ik heb daarvoor natuurlijk de Navier Stokes vergelijkingen gemiddeld, geschaald, getransformeerd en ge-analyseerd en de bodem gemodeleerd.

Allereerst beweegt de waterlijn 2.5 kilometer periodiek op en neer. Netjes iedere 12 uur en 25 minuten. De methode bleek dus ook stabiel. In het complexe model bleken de waarden voor de waterdiepte en de watersnelheid ook realistisch. Verder, de analyse van verschillende natuursomstandigheden levert plausibele resultaten op. Zoals te zien in de plaatjes.

Table of contents

List of Symbols

Symbol	Meaning	SI unit
$D(x,t)$	Depth of the sea	m
$u(x,t)$	Cross-sectionally averaged velocity	m
$h(x)$	Seabed	m
$l(t)$	Length of the basin	m
$\zeta(x,t)$	Deviation of the surface due to tides	m
v_x	Velocity in the x-direction	ms^{-1}
v_y	Velocity in the y-direction	ms^{-1}
v_z	Velocity in the z-direction	ms^{-1}
f_*	Reciprocal Coriolis parameter	rads^{-1}
f	Coriolis parameter	rads^{-1}
g	Gravitational constant	ms^{-2}
$\bar{h_0}$	Parameter to make sure the resistance term stays finite	m
$p(x,y,z,t)$	Pressure	Pa
ρ	Density	kgm^{-3}
$\bar{r}$	Bed friction coefficient	ms^{-1}
U	Characteristic velocity scale	ms^{-1}
A	Amplitude of the periodic forced tide	m
L	Average length of the basin	m
H	Reference height of the sea	m
ν	Kinematic viscosity	$\mathrm{m}^2\mathrm{s}^{-1}$
ω	Angular frequency of the periodic forced tide	rads^{-1}

List of Dimensionless Symbols

Symbol	Meaning
κ	$\frac{gH}{(\omega L)^2}$
h_0	$\frac{\bar{h_0}}{H}$
r	$\frac{\bar{r}}{gH}$

Chapter 1

Introduction

> Imagine you are going to the beach to collect shells. You arrive, but unfortunately there are no shells to be found. A bit disappointed you decide to make the best of your day and just relax. A few hours later, you decide to look again. Luckily, there are now shells to be found! This is because in the hours you relaxed, the sea water level has fallen due to the ebb tide, meaning that the water flows back. This makes the shells visible. Very happily, you return home, with many beautiful shells.

The sea is massive. This thesis is only about the shorelines, and then mostly tidal inlets. Tidal inlets are connections between the sea and tides at the coast. The inlet enables the possibility of transport of nutrients, sediment and water between the open sea and the basin closer to the shoreline (Willemsen et al. (2015)). Tidal inlets are often investigated as they are important for the study of ecosystems and the stability of the surrounding shoreline. Changes such as the rise of the sea level or human activities influence the inlets.

The story above is a simple example of the influence of tides. Tides influence where the sea ends. This changes during time. In more physical terms, the boundary between the sea and the shore oscillates in time. Often, in research, instead of taken a moving boundary, just the average point where the sea ends is taken. This results in that physical variables are inadequately described at the shoreline.

Tides are caused by the gravitational forces of the Moon and the Sun. One of the tidal components is caused by the Moon and called the M2 tide. The M2 tide has a period of 12 hours and 25 minutes. The Earth takes 24 hours to rotate around its axis, but since the moon orbits the earth in the same direction, the Earth needs 50 minutes to 'catch up' to the moon. The M2 tide has two high and two low peaks every lunar day (24hours and 50 minutes). Hence the period is 12 hours and 25 minutes. The gravitational forces of the Sun also cause tides, for example S2 tide with a period of 12 hours. However, even though the Sun is heavier, the Sun has less influence on tides compared to the Moon since it is much farther away.

There are two basic tidal patterns around the world. If tides have two highs and two lows of the same magnitude, the patterns is called semidiurnal (semi-daily). Furthermore, a diurnal

pattern has only one high tide and one low tide per day. For the shoreline of the Netherlands the M2 tide is the biggest, causing the Netherlands to have semidiurnal tides.

Tides are only one of the many factors that influence the behaviour of the sea. For example, ocean currents, wind currents, temperature differences and pressure differences all also play a part. However, tides are usually researched since they are the main driver of the behavior and are very predictable. The change of water depth and velocity during time, is usually caused by the astronomicaltide. (National Oceanic and Atmospheric Administration (2007))

1.1 Current research

A lot of research has already been done about the water motion in tidal inlets. For the understanding of the morphodynamics there is: Ter Brake (2010). The book Schuttelaars et al. (2022) is more about the modelling itself and includes a chapter about the wetting and drying simulations of shallow water equations. In Balzano (1998) it is stated that there are three main categories to include moving boundaries: a fixed grid, adaptive grid or a coordinate transformation, and reviews 10 different methods. A coordinate transformation is the least popular method of the three, but is done in Takeda (1984). In that article an implicit time scheme is used. This results in the main research question of this thesis:

> *Q: can a coordinate transformation in combination with a time-explicit method be used to model the moving boundary problem in shallow waters?*

There are four sub questions:

> *Q1: can such a method provide numerically stable results?*
> *Q2: can such a method provide convergent results?*
> *Q3: how does the model behave in the specific case study of the Ameland tidal inlet system?*
> *Q4: how does the model behave for inlet systems with different physical variables?*

1.2 Structure

The structure of the thesis is as follows: in Chapter 2 the shallow water equations are derived, scaled and transformed by the coordinate transformation. In Chapter 3 the numerical method is introduced. Furthermore in Chapter 3 the solution analysis (Fourier analysis) is explained. Then in Chapter 4 the results are discussed, first for the Ameland tidal inlet system and then the model is checked for different parameters that correspond to different inlet systems. In Chapter 5 a conclusion is drawn and further research is discussed.

Chapter 2

Model description

First the geometry is explained, then the shallow water equations are derived. Afterwards, the equations are scaled and a coordinate transformation is done.

2.1 Geometry

The one-dimensional geometry is visualized in Figure 2.1. The tidal inlet considered is rectangular. The seaward side is located at $x = 0$, while the end of the basin is denoted by $x = l(t)$. In Figure 2.1 a cross-sectional view of the inlet is shown. Here $z = H$ is the reference depth of the inlet as if there would be no tides. The sea surface elevation is denoted by $\zeta(x, t)$. The location of the seabed is denoted by $h(x, t)$ and chosen such that $h(0, t) = 0$. The average position of the end of the sea is located at $x = L$. Finally the instantaneous water depth D is defined as $D(x, t) = H + \zeta(x, t) - h(x, t)$, so D is the depth of the sea.

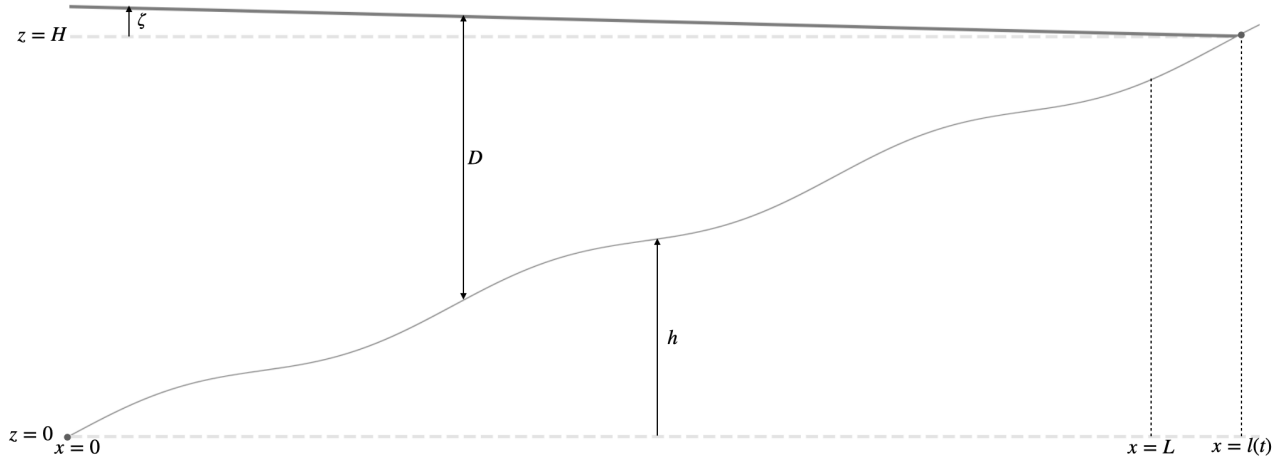

Fig. 2.1 Cross-sectional view of the sea and shoreline

2.2 Equations

To describe the water motion, the continuity equations and Navier-Stokes equations are used for incompressible flow. Incompressible flow is flow where the density ρ is constant. These equations are:

$$\begin{cases} \dfrac{\partial v_x}{\partial x} + \dfrac{\partial v_y}{\partial y} + \dfrac{\partial v_z}{\partial z} = 0, & \text{(2.1a)} \\ \dfrac{\partial v_x}{\partial t} + v_x\dfrac{\partial v_x}{\partial x} + v_y\dfrac{\partial v_x}{\partial y} + v_z\dfrac{\partial v_x}{\partial z} + f_* v_z - f v_y = -\dfrac{1}{\rho}\dfrac{\partial p}{\partial x} + \nu\left(\dfrac{\partial^2 v_x}{\partial x^2} + \dfrac{\partial^2 v_x}{\partial y^2} + \dfrac{\partial^2 v_x}{\partial z^2}\right), & \text{(2.1b)} \\ \dfrac{\partial v_y}{\partial t} + v_x\dfrac{\partial v_y}{\partial x} + v_y\dfrac{\partial v_y}{\partial y} + v_z\dfrac{\partial v_y}{\partial z} + f v_x = -\dfrac{1}{\rho}\dfrac{\partial p}{\partial y} + \nu\left(\dfrac{\partial^2 v_y}{\partial x^2} + \dfrac{\partial^2 v_y}{\partial y^2} + \dfrac{\partial^2 v_y}{\partial z^2}\right), & \text{(2.1c)} \\ \dfrac{\partial v_z}{\partial t} + v_x\dfrac{\partial v_z}{\partial x} + v_y\dfrac{\partial v_z}{\partial y} + v_z\dfrac{\partial v_z}{\partial z} - f_* v_x = -\dfrac{1}{\rho}\dfrac{\partial p}{\partial z} + \nu\left(\dfrac{\partial^2 v_z}{\partial x^2} + \dfrac{\partial^2 v_z}{\partial y^2} + \dfrac{\partial^2 v_z}{\partial z^2}\right). & \text{(2.1d)} \end{cases}$$

For used symbols, see the list of symbols. Following Rozendaal (2019), first the three-dimensional shallow water equations are derived from the Navier Stokes equations. These new equations are then averaged over the depth and width. Then neglecting the viscosity term, the resulting cross-sectionally averaged one-dimensional shallow water equations are obtained:

$$\begin{cases} \dfrac{\partial \zeta}{\partial t} - \dfrac{\partial h}{\partial t} + \dfrac{\partial}{\partial x}[(H + \zeta - h)u] = 0, & \text{(2.2a)} \\ \dfrac{\partial u}{\partial t} + u\dfrac{\partial u}{\partial x} = -g\dfrac{\partial \zeta}{\partial x} - \dfrac{\bar{r}u}{H + \zeta - h + \bar{h_0}}, & \text{(2.2b)} \end{cases}$$

where the seabed $h(x)$ is prescribed and assumed fixed in time, u is the cross-sectionally (over y and z) averaged velocity in the x-direction, $\bar{r}$ is the friction coefficient between the water and the seabed and $\bar{h_0}$ is a positive constant such that the last term of Equation (2.2b) (that models the effects of bed friction) is always finite.

Using the definition of $D(x,t) = H + \zeta(x,t) - h(x)$, the system of equations (2.2) can be rewritten as:

$$\begin{cases} \dfrac{\partial D}{\partial t} + \dfrac{\partial}{\partial x}(Du) = 0, & \text{(2.3a)} \\ \dfrac{\partial u}{\partial t} + u\dfrac{\partial u}{\partial x} = -g\dfrac{\partial D}{\partial x} - g\dfrac{\partial h}{\partial x} - \dfrac{\bar{r}u}{D + \bar{h_0}}. & \text{(2.3b)} \end{cases}$$

Where $x \in [0, l(t)]$ and $t > 0$. Note that $l(t)$ is not taken constant in time. Hence an extra condition is needed for $l(t)$. This is the kinematic condition which states that a particle that is on the interface between the sea and the shore, never leaves that interface. Or in other words $\dfrac{\mathrm{d}l}{\mathrm{d}t}$ is equal to the velocity of that particle: $\dfrac{\mathrm{d}l}{\mathrm{d}t} = u(l(t), t)$ (Takeda (1984)).

At $x = 0$, a semidiurnal tide for the sea surface elevation is prescribed, specifically $\zeta(0,t) = A\cos(\omega t)$. Here A the amplitude and ω the angular frequency of the M2 tide. At the shoreline, $x = l(t)$, there should not be any water flowing through the boundary. Therefore

the mass transport at $x = l(t)$ must vanish. This results in the following boundary conditions:

$$\begin{cases} D = A\cos(\omega t) + H & \text{at } x = 0, \quad (2.4a) \\ Du = 0 & \text{at } x = l(t). \quad (2.4b) \end{cases}$$

Furthermore, as initial conditions it is prescribed:

$$\begin{cases} u = 0 & \text{at } t = 0, \quad (2.5a) \\ D = H + A - h(x) & \text{at } t = 0. \quad (2.5b) \end{cases}$$

Because of the presence of the semidiurnal tide at $x = 0$, which states that $\zeta(0, t) = A\cos(\omega t)$, the choice of initial conditions is not that important: the system eventually reaches a periodic equilibrium state.

2.3 Non-dimensionalization

Non-dimensionalization and scaling are used to simplify equations and to easily see the relative importance of the various terms. The dimensionless variables are defined with an asterisk(*) and defined as:

$$\begin{cases} t = \dfrac{1}{\omega} t^*, & (2.6a) \\ x = Lx^*, & (2.6b) \\ D = HD^*, & (2.6c) \\ u = Uu^*, & (2.6d) \\ h = Hh^*, & (2.6e) \\ \bar{h_0} = Hh_0^*, & (2.6f) \\ l = Ll^*, & (2.6g) \\ \bar{r} = \omega H r^*. & (2.6h) \end{cases}$$

Due to the non-dimensionalization the derivatives also change:

$$\begin{cases} \dfrac{\partial}{\partial t} = \omega \dfrac{\partial}{\partial t^*}, & (2.7a) \\ \dfrac{\partial}{\partial x} = \dfrac{1}{L} \dfrac{\partial}{\partial x^*}. & (2.7b) \end{cases}$$

Substituting these new variables into Equation (2.3a) results in:

$$\omega H \frac{\partial D^*}{\partial t^*} + \frac{HU}{L} \frac{\partial}{\partial x^*}(D^* u^*) = 0. \quad (2.8)$$

The characteristic velocity scale is chosen as $U = \omega L$ due to the mass balance.

The conservation of momentum equation (2.3b) reads:

$$\omega U \frac{\partial u^*}{\partial t^*} + \frac{U^2}{L} u^* \frac{\partial u^*}{\partial x^*} = -\frac{gH}{L}\left(\frac{\partial D^*}{\partial x^*} + \frac{\partial h^*}{\partial x^*}\right) - \omega U \frac{r^* u^*}{D^* + h_0^*}. \quad (2.9)$$

Dividing by ωU and defining $\kappa = \dfrac{gH}{(\omega L)^2}$ results in:

$$\frac{\partial u^*}{\partial t^*} + u^* \frac{\partial u^*}{\partial x^*} = -\kappa\left(\frac{\partial D^*}{\partial x^*} + \frac{\partial h^*}{\partial x^*}\right) - \frac{r^* u^*}{D^* + h_0^*}. \tag{2.10}$$

For simplicity in notation, from now on, the * are dropped from the equations. The non-dimensionalization results in the following system of equations:

$$\begin{cases} \dfrac{\partial D}{\partial t} + \dfrac{\partial}{\partial x}(Du) = 0, & \text{(2.11a)} \\ \dfrac{\partial u}{\partial t} + u\dfrac{\partial u}{\partial x} = -\kappa\left(\dfrac{\partial D}{\partial x} + \dfrac{\partial h}{\partial x}\right) - \dfrac{ru}{D + h_0}, & \text{(2.11b)} \\ \dfrac{\mathrm{d}l}{\mathrm{d}t} = u(l(t), t). & \text{(2.11c)} \end{cases}$$

The corresponding boundary conditions (where also the * is removed for simplicity) are:

$$\begin{cases} D = \dfrac{A}{H}\cos(t) + 1 & \text{at } x = 0, \quad \text{(2.12a)} \\ Du = 0 & \text{at } x = l(t). \quad \text{(2.12b)} \end{cases}$$

2.4 Coordinate transformation

In the system of equations (2.11) and (2.12), the location of the landward boundary $x = l(t)$ depends on time. There are multiple ways to approach this problem, examples are using moving grids or a coordinate transformation, see Balzano (1998). Here, the latter has been chosen. The coordinate transformations are $\hat{t} = t$ and $\hat{x} = \dfrac{x}{l(t)}$ such that $0 \leq x \leq l(t)$ transforms into $0 \leq \hat{x} \leq 1$. Let $\hat{l}(\hat{t}) = l(t)$, $\hat{u}(\hat{x}, \hat{t}) = u(x, t)$, $\hat{h}(\hat{x}, \hat{t}) = h(x, t)$ and $\hat{D}(\hat{x}, \hat{t}) = D(x, t)$. The equations in the new coordinates read:

$$\begin{cases} \dfrac{\partial \hat{D}}{\partial \hat{t}} - \dfrac{\hat{x}}{\hat{l}}\dfrac{\mathrm{d}\hat{l}}{\mathrm{d}\hat{t}}\dfrac{\partial \hat{D}}{\partial \hat{x}} + \dfrac{1}{\hat{l}}\dfrac{\partial}{\partial \hat{x}}(\hat{D}\hat{u}) = 0, & \text{(2.13a)} \\ \dfrac{\partial \hat{u}}{\partial \hat{t}} - \dfrac{\hat{x}}{\hat{l}}\dfrac{\mathrm{d}\hat{l}}{\mathrm{d}\hat{t}}\dfrac{\partial \hat{u}}{\partial \hat{x}} + \dfrac{\hat{u}}{\hat{l}}\dfrac{\partial \hat{u}}{\partial \hat{x}} = -\dfrac{\kappa}{\hat{l}}\left(\dfrac{\partial \hat{D}}{\partial \hat{x}} + \dfrac{\partial \hat{h}}{\partial \hat{x}}\right) - \dfrac{r\hat{u}}{\hat{D} + h_0}, & \text{(2.13b)} \\ \dfrac{\mathrm{d}\hat{l}}{\mathrm{d}\hat{t}} = \hat{u}, & \text{(2.13c)} \end{cases}$$

where it is used that:

$$\begin{cases} \dfrac{\partial}{\partial t} = \dfrac{\partial \hat{t}}{\partial t}\dfrac{\partial}{\partial \hat{t}} + \dfrac{\partial \hat{x}}{\partial t}\dfrac{\partial}{\partial \hat{x}} = \dfrac{\partial}{\partial \hat{t}} - \dfrac{\hat{x}}{\hat{l}}\dfrac{\mathrm{d}\hat{l}}{\mathrm{d}\hat{t}}\dfrac{\partial}{\partial \hat{x}}, & \text{(2.14a)} \\ \dfrac{\partial}{\partial x} = \dfrac{1}{\hat{l}(\hat{t})}\dfrac{\partial}{\partial \hat{x}}. & \text{(2.14b)} \end{cases}$$

The transformed boundary conditions are:

$$\begin{cases} \hat{D} = \dfrac{A}{H}\cos(\hat{t}) + 1 & \text{at } \hat{x} = 0, \quad \text{(2.15a)} \\ \hat{D}\hat{u} = 0 & \text{at } \hat{x} = 1. \quad \text{(2.15b)} \end{cases}$$

Again for simplicity in notation, dropping all the $\hat{\cdot}$, the system of equations becomes:

$$\begin{cases} \dfrac{\partial D}{\partial t} - \dfrac{x}{l}\dfrac{\mathrm{d}l}{\mathrm{d}t}\dfrac{\partial D}{\partial x} + \dfrac{1}{l}\dfrac{\partial}{\partial x}(Du) = 0, & (2.16a) \\ \dfrac{\partial u}{\partial t} - \dfrac{x}{l}\dfrac{\mathrm{d}l}{\mathrm{d}t}\dfrac{\partial u}{\partial x} + \dfrac{u}{l}\dfrac{\partial u}{\partial x} = -\dfrac{\kappa}{l}(\dfrac{\partial D}{\partial x} + \dfrac{\partial h}{\partial x}) - \dfrac{ru}{D+h_0}, & (2.16b) \\ \dfrac{\mathrm{d}l}{\mathrm{d}t} = u(1,t). & (2.16c) \end{cases}$$

with boundary conditions:

$$\begin{cases} D = \dfrac{A}{H}\cos(t) + 1 & \text{at } x = 0, \quad (2.17a) \\ Du = 0 & \text{at } x = 1. \quad (2.17b) \end{cases}$$

Chapter 3

Solution method

Discretized forms of equations (2.16) and (2.17) are being solved numerically. In this chapter the numerical method is introduced. Furthermore the method is checked to be stable and the convergence is briefly checked. The Fourier transformation (to analyse the solution) is explained.

3.1 Numerical method

The numerical method chosen to discretize and numerically solve the equations (2.16) and (2.17) is the Lax-Friedrichs finite difference method (Press et al. (1995)). This method is very similar to the FTCS (Forward in time, centered in space) method. The method is chosen due to its simplicity for the spatial-discretization. Furthermore, the method is explicit, rather than implicit, so it is easier to implement and has a lower computational cost. It should be noted however, that the Lax-Friedrichs method is known to be dissipative and dispersive. Therefore a grid refinement study will be performed.

For the spatial coordinate the grid is discretized by $x_j = j\Delta x$ for $1 \leq j \leq M$, and for the time by $t_n = n\Delta t$ for $n > 0$.

The Lax-Friedrichs method uses central differences for the discretization in space:

$$\frac{\partial f}{\partial x} = \frac{f_{j+1}^n - f_{j-1}^n}{2\Delta x}, \tag{3.1}$$

where f_j^n is the function $f(x,t)$ evaluated at time t_n and place x_j. The discretization in time is similar to that of the Forward Euler method:

$$\frac{\partial f}{\partial t} = \frac{f_j^{n+1} - f_j^n}{\Delta t}. \tag{3.2}$$

However due to numerical stability, the term f_j^n in Eq.(3.2) is replaced by $\frac{1}{2}(f_{j+1}^n + f_{j-1}^n)$:

$$\frac{\partial f}{\partial t} = \frac{f_j^{n+1} - \frac{1}{2}(f_{j+1}^n + f_{j-1}^n)}{\Delta t}. \tag{3.3}$$

For a one dimensional partial differential equation of $y(x,t)$:

$$\frac{\partial y}{\partial t} + \frac{\partial f(y)}{\partial x} = R(x,t), \tag{3.4}$$

the Lax-Friedrichs method therefore results in (Hudson (1998)):

$$y_j^{n+1} = \frac{1}{2}(y_{j+1}^n + y_{j-1}^n) - \frac{\Delta t}{2\Delta x}(f(y_{j+1}^n) - f(y_{j-1}^n)) + \Delta t R_j^n, \tag{3.5}$$

where R_j^n is the source term. In the system of equations (Eq. 2.16) the source term will be discretized by central differences and the time discretization by the earlier given scheme: (3.3).

Since $l(t)$ does not depend on the spatial coordinate it only has a temporal discretization. Again the same temporal discretization is used, where it should be noted that $\frac{1}{2}(l_{j+1}^n + l_{j-1}^n) = l_j^n$. So for the discretization of $\frac{\mathrm{d}l}{\mathrm{d}t}$ using method (3.3) is the same as using Forward Euler. For the system it is checked that it is still stable.

In Figure 3.1 the stencil of the Lax-Friedrichs method is shown where $t = n\Delta t$ and $x = j\Delta x$.

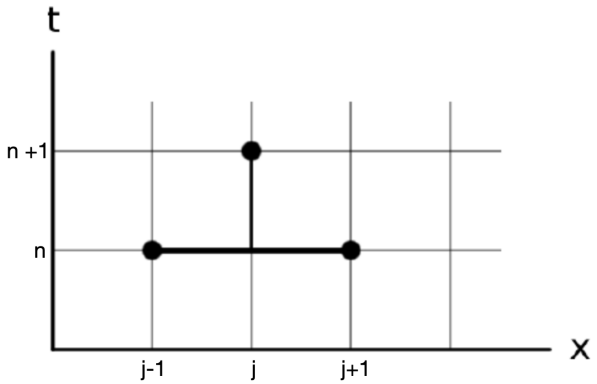

Fig. 3.1 Stencil of the Lax-Friedrichs method

Using the above definition the discrete system of equations (2.16) reads:

$$\begin{aligned} D_j^{n+1} = &\frac{1}{2}(D_{j+1}^n + D_{j-1}^n) \\ &+ \frac{x_j}{l^n}(l^{n+1} - l^n)\frac{D_{j+1}^n - D_{j-1}^n}{2\Delta x} - \frac{\Delta t}{2\Delta x}\frac{}{l^n}(D_{j+1}^n u_{j+1}^n - D_{j-1}^n u_{j-1}^n), \end{aligned} \tag{3.6}$$

and

$$\begin{aligned} u_j^{n+1}(1 + \Lambda\Delta t) = &\frac{u_{j+1}^n + u_{j-1}^n}{2} \\ &+ \frac{\Delta t}{2l^n\Delta x}\Big((x_j\frac{l^{n+1} - l^n}{\Delta t} - u_j^n)(u_{j+1}^n - u_{j-1}^n) - \kappa(D_{j+1}^n - D_{j-1}^n + h_{j+1}^n - h_{j-1}^n)\Big), \end{aligned} \tag{3.7}$$

with $\Lambda = \dfrac{r}{D_j^{n+1} + h_0}$.

In discretizing the last term of the right hand side of Equation (2.16b) an implicit scheme is chosen. This is to prevent a positive feedback loop where a decreasing u results in a decrease of $\dfrac{\partial u}{\partial t}$ (causing u to decrease again) . This positive feedback loop would make the system unstable.

The final Equation of (2.16), reads in discretized form:

$$l^{n+1} = l^n + \Delta t u_M^n. \tag{3.8}$$

At the boundaries, forward/backward differences are used to obtain the velocity $u(x,t)$. The forward/backward differences are second order, so the same accuracy is obtained as with the central differences used in (3.6) and (3.7). At the boundaries for the time integration Forward Euler is used since it is not possible to replace f_j^n by $\frac{1}{2}(f_{j+1}^n + f_{j-1}^n)$ where $j = 0$ or $j = M$. The resulting boundary conditions read:

$$\begin{cases} u_0^{n+1}(1 + \Lambda\Delta t) = u_0^n - \dfrac{\Delta t}{2l^n\Delta x}\Big(u_0^n(-3u_0^n + 4u_1^n - u_2^n)\Big) \\ - \dfrac{\Delta t}{2l^n\Delta x}\Big(\kappa(-3D_0^n + 4D_1^n - D_2^n - 3h_0^n + 4h_1^n - h_2^n)\Big) \end{cases} \tag{3.9}$$

$$\begin{cases} u_M^{n+1}(1 + \Lambda\Delta t) = u_M^n - \dfrac{\Delta t}{2l^n\Delta x}\Big((u_0^n - \dfrac{l^{n+1} - l^n}{\Delta t})(3u_M^n - 4u_{M-1}^n + u_{M-2}^n)\Big) \\ - \dfrac{\Delta t}{2l^n\Delta x}\Big(\kappa(3D_M^n - 4D_{M-1}^n + D_{M-2}^n + 3h_L^n - 4h_{M-1}^n + h_{M-2}^n)\Big) \end{cases} \tag{3.10}$$

For the depth $D(x,t)$ the discretized boundary conditions read:

$$\begin{cases} D_0^{n+1} = 1 + \dfrac{A}{H}\cos((n+1)\Delta t, & \text{(3.11a)} \\ D_M^{n+1} = 0. & \text{(3.11b)} \end{cases}$$

3.1.1 Stability

For the equations (3.6) and (3.7) the system is not stable for all chosen Δt and Δx. Since the system of equations considered is nonlinear, a full analysis of the stability of the scheme above is outside the scope of this thesis. Here I will consider the stability using the Courant-Friedrichs-Lewy (CFL) condition. This is choice is further explained in the Appendix.

The CFL condition is a condition for numerical methods involving waves. It states that the distance travelled for a point on the wave in one timestep should be smaller than Δx (one gridstep). Therefore the information does not travel further than one neighbouring cell. The distance travelled in one unit of time is the wave velocity, which in shallow water is given by $\sqrt{gH}$.

For the non dimensionalization this means $\sqrt{gH}\dfrac{\Delta t}{\Delta x} \leq 1$. In the nondimensional frame the conditions become $\sqrt{gH}\dfrac{1}{\omega L}\dfrac{\Delta t}{\Delta x} = \sqrt{\kappa}\dfrac{\Delta t}{\Delta x} \leq 1$. The CFL is not necessarily a sufficient

condition. In the remainder of this thesis it is chosen that:

$$\Delta t \leq \frac{0.9}{\sqrt{\kappa}}\Delta x. \tag{3.12}$$

3.1.2 Choice of h_0

The parameter h_0 in Eq.(2.16) ensures that the term $\frac{ru}{D+h_0}$ stays finite for $D = 0$. The value of h_0 is not known. Furthermore, it can be seen as a parameter that takes the neglected effects into account (when deriving the one dimensional shallow water equations). A possible choice for h_0 can be the size of a water molecule. However, this would mean that h_0 is of order 10^{-10} in the scaled domain, which would still cause the system to be unstable. Another choice would be the capillary length, which is the length scale associated with water for which the gravity and surface tension are balanced. For water this is 3mm, so the scaled variable $h_0 = 0.00025$. Another option is to make h_0 bigger, for example 10 times the capillary length.

Since the Lax-Friedrichs method is known to be dissipative, it is important to have a fine grid. Take $M + 1$ the number of grid points. Then $\Delta x = \frac{1}{M}$. Due to the stability criterion $\frac{\Delta t}{\Delta x} < \frac{0.9}{\sqrt{\kappa}}$, increasing M means decreasing Δt. In the sections below, for the two given choices of h_0, results are compared for different M. It should be noted that Δt is chosen such that $\frac{\Delta t}{\Delta x}$ is the same for different values of M.

The various choices of M range from $M = 100$ to $M = 5000$. Increasing M even more results in too long runtimes, so this is not done.

3.1.2a $h_0 = 0.00025$

The first option is $h_0 = 0.00025$, i.e. h_0 is related to the capillary length scale. Comparing the results for different M is difficult since both $u(x,t)$ and $D(x,t)$ depend on space and time. To quickly compare the results, the resulting temporally varying length $l(t)$ of the inlet is plotted for various M in Figure 3.2. As can be seen in this figure, there is a big difference for different M. For the range of M values considered, refining the grid did not result in converged results. For further research, a more refined grid could be taken to check the convergence better but for now the computational time is too long for this.

3.1.2b $h_0 = 0.0025$

A second choice of h_0 is $h_0 = 0.0025$ (dimensionfull this corresponds to a value of 3 cm). So h_0 is ten times as big as the capillary length. If again the length is plotted for different M, the resulting $l(t)$ are now very similar to each other (see Figure 3.3). Zooming in (Figure 3.4), there are still some small differences, but these clearly get smaller for larger M.

Plotting the maximum/minimum velocity at different grid cells, there is still a difference in amplitude for different M (Figures 3.5 and 3.6).

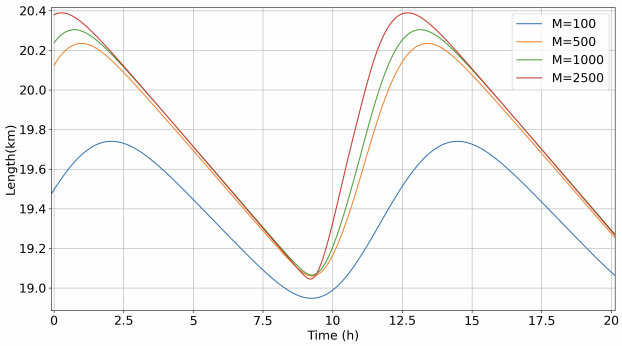

Fig. 3.2 Length of the basin for different M and $h_0 = 0.00025$.

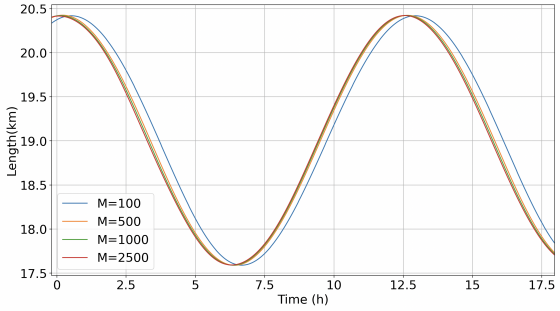

Fig. 3.3 Length of the basin for different M and $h_0 = 0.0025$.

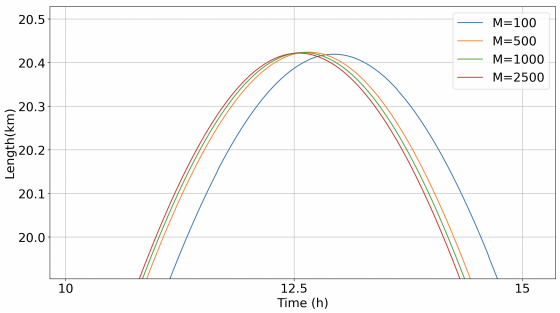

Fig. 3.4 Zoomed in length of the basin for different M and $h_0 = 0.0025$.

The question is if the velocity amplitudes eventually converge for bigger M. For this, the maximum amplitude for each M of Figure 3.5 and minimum amplitude for each M of Figure 3.6 are plotted with a curve fit of the form $y = \frac{a}{M^d + b} + c$. The results are in Figures 3.7 and 3.8. Since $d \geq 0$ for both plots, the amplitude converges to c for M to infinity. So the amplitudes do converge. For the maximum velocity this is $c_{\max} = 0.170\text{m/s}$ and for the minimum velocity: $c_{\min} = -0.180\text{m/s}$. Both of these values are similar to the expected velocity (by Rozendaal (2019) and Ter Brake (2010)), which is $\frac{A\omega L}{H} \approx 0.186\text{m/s}$.

Since $h_0 = 0.0025$ results in much better behaviour of the system, this is the value of h_0 that will be chosen. Furthermore in this thesis, due to the runtimes, $M = 500$ is used.

3.2 Fourier analysis

A harmonic wave can be characterized by its period (or frequency), the amplitude and the phase. For any function a Fourier analysis can be used to see the underlying sines/cosines that build up this function. Fourier analysis is a mathematical technique to decompose a signal into a sum of harmonic waves by transforming a function from the time domain into the frequency domain. The function is broken down into repetitive wave forms and these can be easily analyzed.

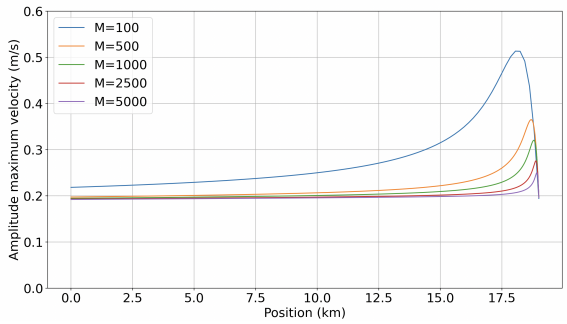

Fig. 3.5 Maximum velocity for different M at different locations and $h_0 = 0.0025$.

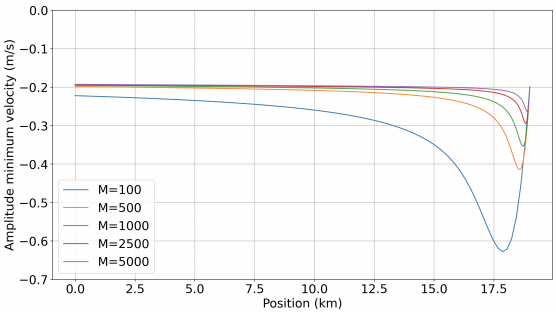

Fig. 3.6 Minimum velocity for different M at different locations and $h_0 = 0.0025$.

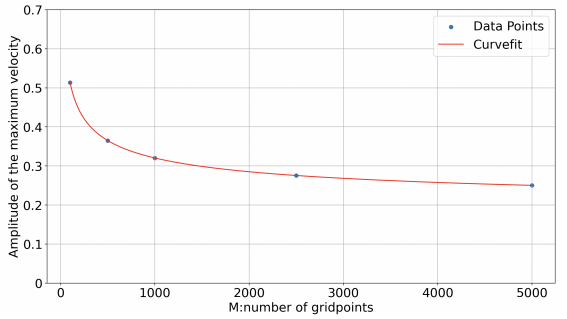

Fig. 3.7 Maximum amplitude of the velocity in time and space for different M and $h_0 = 0.0025$.

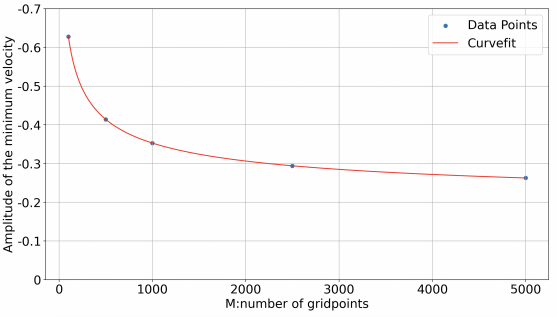

Fig. 3.8 Minimum amplitude of the velocity in time and space for different M and $h_0 = 0.0025$.

There is a continuous and discrete Fourier transform. Since in the numerical simulations the time domain is discretized, a discrete Fourier transform (DFT) is used. For an input $y_0, y_1, ..., y_{N-1}$ with $y_n = y(t_n)$ the sequence is transformed in $Y_k := Y_0, Y_1, Y_2, ..., Y_{N-1}$ by the discrete Fourier transform, that is given by:

$$Y_k = \sum_{n=0}^{N-1} y_n e^{-i2\pi \frac{k}{N} n}. \tag{3.13}$$

The frequency bins depend on the sample frequency f_s. The kth frequency bin is $k\frac{f_s}{N}$, with $k \in [0, N-1]$. Note that the Y_k are periodic.

The amplitude in the Fourier spectrum is calculated by $\sqrt{\Re(Y_k)^2 + \Im(Y_k)^2}$ and gives information about the amplitude in the time domain. If the amplitude is normalized by the number of sample points, it is equal to the amplitude of the input. Knowing the amplitude, phase and the corresponding frequency, the original signal can be reconstructed.

Several problems can occur with Fourier transforms, one of them being aliasing. This happens when a signal is undersampled, and the original wave can not be reconstructed. An example

is shown in Figure 3.9.

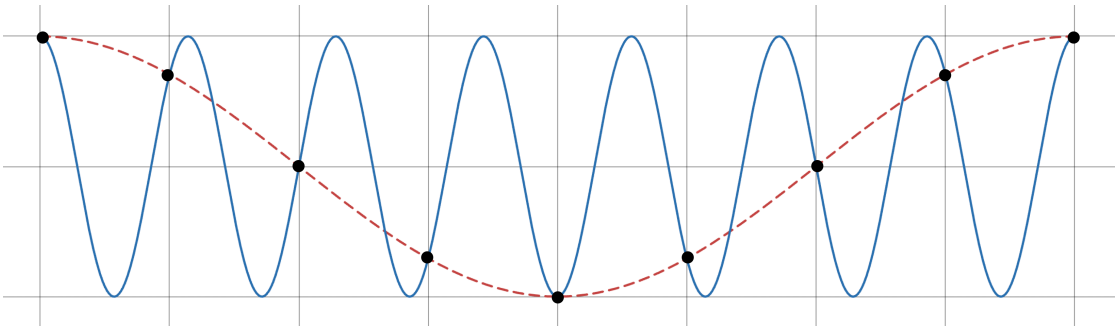

Fig. 3.9 Aliasing, if the signal (blue line) is undersampled (black dots) the reconstructed signal (dotted red line) has a lower frequency.

To explain this further, define the Nyquist frequency as: $f_c = \frac{1}{2} f_s$ with f_s the sample frequency. Now there are two possibilities. The first one is that the input signal is bandwidth limited with all frequencies $\leq f_{max}$. Then if $f_c > f_{max}$ the function can be completely reconstructed. However, if a input signal is not bandwidth limited (i.e. $f_{max} \to \infty$), the frequencies outside of the range $[-f_c, f_c]$ are transformed back into this range (see Figure 3.10). The frequencies are mirrored in f_c. So for example if $f_c = 50Hz$ and you want to sample a signal of $f = 70Hz$ then this is out of the range. The peak you will see, due to aliasing, is at $2f_c - f = 30Hz$.

By looking at the Fourier transform of a sampled signal, if the amplitudes approach 0 at $\pm f_c$ then there is no aliasing, whereas if the amplitudes approach finite values there is aliasing. Aliasing can be solved by filtering the signal before sampling. (Press et al. (1995))

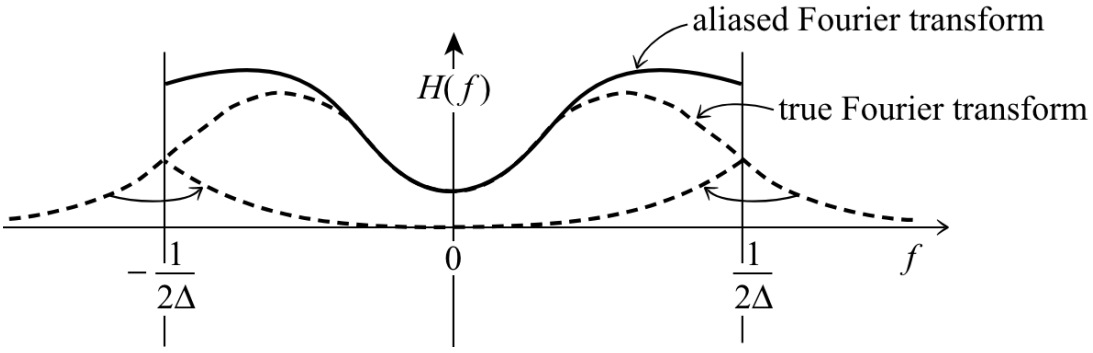

Fig. 3.10 Overlap of the frequencies due to aliasing in the frequency domain (Press et al. (1995))

3.2.1 Domain

The Fourier transformation is taken in the fixed domain. So for different fixed dimensional locations the Fourier coefficients are calculated. Here a problem arises. The depth and velocity are calculated for different x in the moving domain. So interpolation is needed to obtain the values of the depth and velocity fixed locations. The SciPy library in Python is used for the interpolation, using linear form.

3.2.2 Python

The Discrete Fourier transform (3.13) is slow, it has a computational complexity of $\mathcal{O}(N^2)$ (since there are N outputs, and for each output there is a sum of N terms). Therefore a Fast Fourier transform (FFT) is used. A FFT is an algorithm such that the Fourier transformation is computed faster. When a FFT is used, it is most optimal to have an input size of $2^{\bar{N}}$ with $\bar{N}$ an integer. In this report the FFT implementation of the Python library Scipy is used.

If the input is real, the Fourier transform is symmetric. So $Y_k = Y^*_{-k \bmod N}$ where Y^* is the complex conjugate. In other words, there is a DC component, positive and negative frequencies. The amplitude of the negative frequencies is equal to the amplitude of the positive component. The phases are equal (but inverted). Therefore it is possible to only look at the DC component and positive frequencies to get all the information you need. This is called the Real Fast Fourier transform (RFFT).

To reconstruct the original signal the phase and amplitude for different frequencies are needed. The phase is known, but for the amplitudes only half of the spectrum is taken. Therefore, for all frequencies except the DC component ($f = 0$), the normalized amplitude is multiplied by 2 while the phase remains unchanged.

Chapter 4

Results

In this chapter the results are discussed. In section 4.1 physical characteristics of the Ameland inlet system are used. First a simplified model without non-linearities is analytically solved. Then, the full non-linear model is solved numerically. In section 4.2 different physical characteristics are varied to investigate the sensitivity to parameter changes.

4.1 The short basin limit

The values of the parameters that make the variables dimensionless (see Eq.(2.6)) depend on the precise characteristics (geometry and physics) of the tidal inlet system. In this report the Ameland tidal inlet system is used as the default inlet, since this inlet is one of the most natural inlets in the Netherlands. That means that the tidal system has remained relatively untouched preserving its original state (Van der Vegt (2006)). The parameters of the inlet system are given in Table 4.1 (Rozendaal (2019)).

Channel	Tide	Parameters	Dimensionless	Numerical
L =1.9·10^{4}m	$\omega = 1.4{\cdot}10^{-4}\text{rads}^{-1}$	$g = 9.81\ \text{ms}^{-2}$	$\kappa \sim 1.7{\cdot}10^1$	$\Delta x = 0.002$
H=12m	$A = 0.84\text{m}$	$\bar{h_0} = 3\text{cm}$	$h_0 = 0.0025$	$\Delta t = 0.0004$
		$\bar{r} = 4 \cdot 10^{-4}\text{ms}^{-1}$	$r = 0.24$	

Table 4.1 Characteristics of the Ameland tidal inlet system.

For simplicity the seabed will be modelled as a straight slope in the original frame. So in the dimensional frame $h(x) = \frac{H}{L}x$ and in the dimensionless frame this reduces to $h_{\text{non-dim}}(x) = x$. In the transformed coordinate frame this will be $h_{\text{transformed}}(x) = xl(t)$.

4.1.1 Simplified model

For a general understanding of the system, the dominant term is the most important. Looking at equation (2.16b) and noting that $\kappa \gg 1$ (see Table 4.1), the momentum equation can be approximated as:

$$-\frac{\kappa}{l}(\frac{\partial D}{\partial x} + \frac{\partial h}{\partial x}) = 0. \tag{4.1}$$

Hence it follows that:

$$\frac{\partial D}{\partial x} + \frac{\partial h}{\partial x} = 0 \tag{4.2}$$

Using that $h = h_{\text{transformed}} = xl(t)$ it is found that the resulting the water depth is $D(x,t) = -xl(t) + f(t)$. Using the boundary condition (2.17a) the final result is:

$$D(x,t) = 1 - l(t)x + \frac{A}{H}\cos(t). \tag{4.3}$$

Since it holds that $D = 0$ at the landward boundary $x = 1$, it follows that:

$$l(t) = 1 + \frac{A}{H}\cos(t). \tag{4.4}$$

Using equation (2.16a) and boundary condition (2.17b), the velocity can be calculated, resulting in:

$$u(x,t) = -\frac{A}{H}\sin(t). \tag{4.5}$$

Transforming these equations back to the original geometry results in:

$$\begin{cases} D(x,t) = H - \dfrac{H}{L}x + A\cos(\omega t), & \text{(4.6a)} \\ u(x,t) = -\dfrac{LA\omega}{H}\sin(\omega t), & \text{(4.6b)} \\ l(t) = L + L\dfrac{A}{H}\cos(\omega t). & \text{(4.6c)} \end{cases}$$

In Eq.(4.6) $u(x,t)$ is not dependent on x. Since $u(L,t) = \dfrac{\mathrm{d}l}{\mathrm{d}t}$ due to the kinematic boundary condition, $u(x,t) = \dfrac{\mathrm{d}l}{\mathrm{d}t}$ for all x.

4.1.2 Ameland inlet system

In Figure 4.1 the length of the system is plotted. The green line is the numerical solution of the full model, the gray line is the analytical solution of the simplified model of section 4.1.1. As can be seen in the plot, after approximately 12.5 hours the system becomes periodic with a period of 12 hours and 25 minutes. This Figure shows that the varying length of the nonlinear model is very similar to that of the simplified model.

In Figure 4.2a the results are shown for the depth and in Figure 4.2b the results for the velocity. The blue/red line represent the numerical model and the gray line represents the solution of the simplified model of section 4.1.1. In the Figures one period is shown of 12 hours and 25 minutes, where the system is already stabilized. For the depth a side view of the sea is shown, where the brown line is the seabed. Furthermore, the depth $D(x,t)$ is only plotted at the end of the basin, this is because only there the influence of the nonlinearities can be seen. At the seaward side of the basin, the solution is very similar to the analytical solution. At the landward side there are differences between the solutions of the simple and full model. The depth slightly bends and the velocity reaches its maximum/minimum (seen by the peaks and valleys). These differences showcase the nonlinearities.

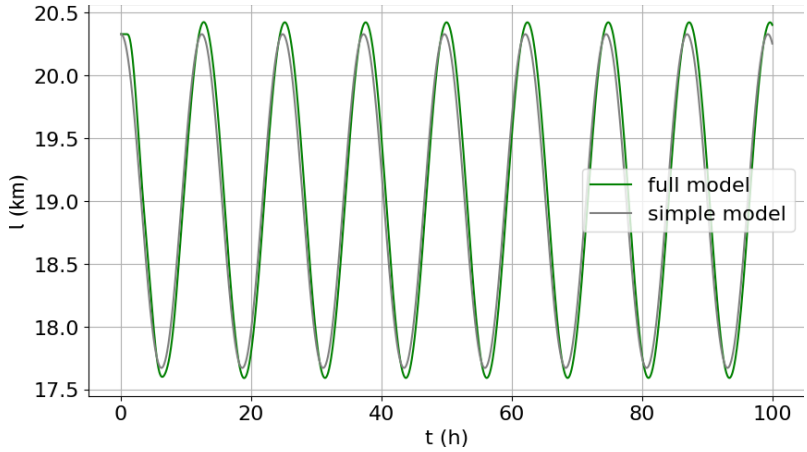

Fig. 4.1 Length of the basin. The green line is the full model calculated numerically whereas the grey line is the simplified model calculated analytically.

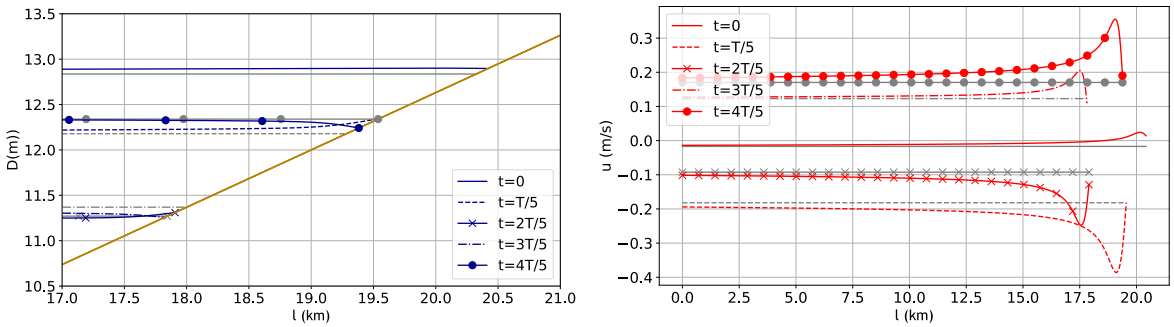

(a) $D(x,t)$ for the model.

(b) $u(x,t)$ for the model.

Fig. 4.2 The length l of the basin as a function of time t for varying parameters.

4.1.3 Fourier analysis

As mentioned before, for the Fourier analysis it is most optimal to have input size $2^{\bar{N}}$ with $\bar{N}$ an integer. In this report there are 2^{14} samples in 50 hours of data. The 50 hours is in the dimensionfull domain. Therefore the sample frequency in the real domain is $f_s = 0.09$Hz. In the dimensionless domain this is a sample frequency of $f_s = 655$Hz. Thus the Nyquist frequency in the dimensionless domain is $f_c = 328$Hz

In the frequency spectrum a few things are to be expected. There is a periodic forcing at $x = 0$ with frequency $\frac{1}{2\pi}$, so for this frequency a peak is expected. Higher harmonic waves are suspected to be generated due to the nonlinear terms of the Navier Stokes equations and due to the varying length. The higher harmonics would therefore have frequencies $\frac{1}{\pi}, \frac{3}{2\pi}, \frac{2}{\pi}$... in the dimensionless domain. These frequencies match with the M4 ($f = \frac{1}{\pi}$), M6 ($f = \frac{3}{2\pi}$) and M8 ($f = \frac{2}{\pi}$) tides of the moon in the dimensionfull domain.

As defined before $D(x,t) = \zeta(x,t) + H - h(x)$. So for the depth the $\zeta(x,t)$ component depends on time, but $H - h(x)$ is a constant in time. This causes a corresponding DC component, which will decrease for x closer to the landward side.

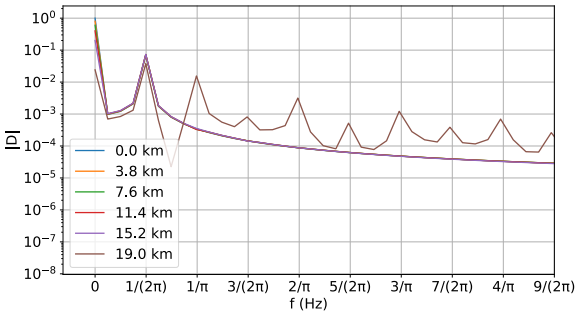

Fig. 4.3 Frequency spectrum of $D(x,t)$

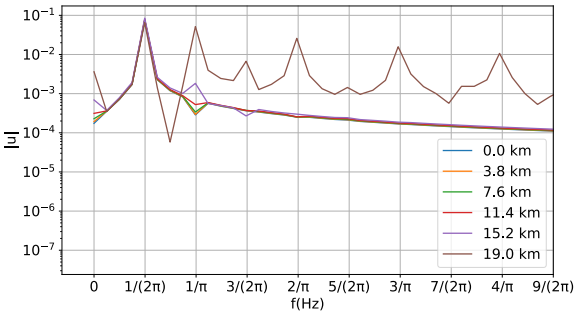

Fig. 4.4 Frequency spectrum of $u(x,t)$

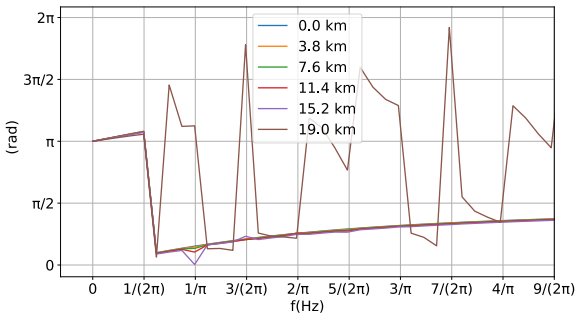

Fig. 4.5 Phase spectrum of $D(x,t)$

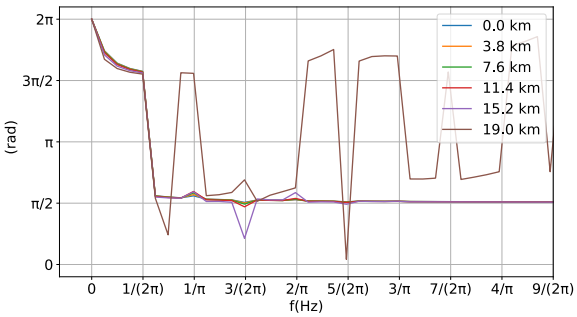

Fig. 4.6 Phase spectrum of $u(x,t)$

In Figures 4.3 and 4.4 the frequency spectrum is plotted for different locations. As can be seen clearly the first three peaks are at $0, \frac{1}{2\pi}$ and $\frac{1}{\pi}$. There are more peaks at $\frac{3}{2\pi}, \ldots$ but these have a very small amplitude. For $x = 19$km these peaks can be seen. There the nonlinearities are more clear since the influence of drying and wetting is felt.

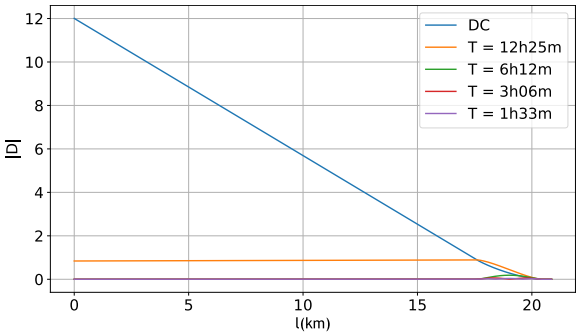

Fig. 4.7 Amplitude of different frequencies for $D(x,t)$.

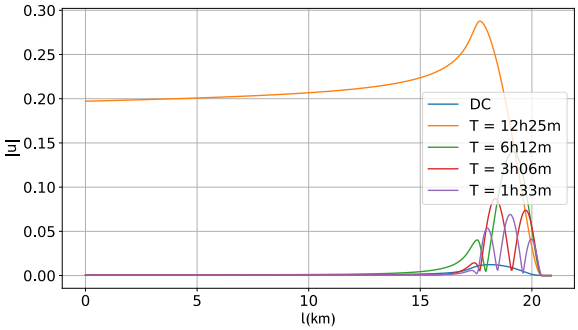

Fig. 4.8 Amplitude of different frequencies for $u(x,t)$.

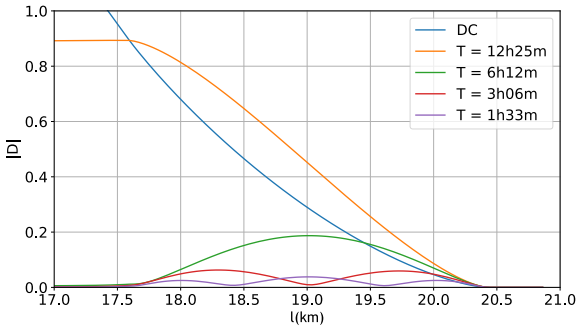

Fig. 4.9 Amplitude of different frequencies for $D(x,t)$ zoomed in at the end of the basin.

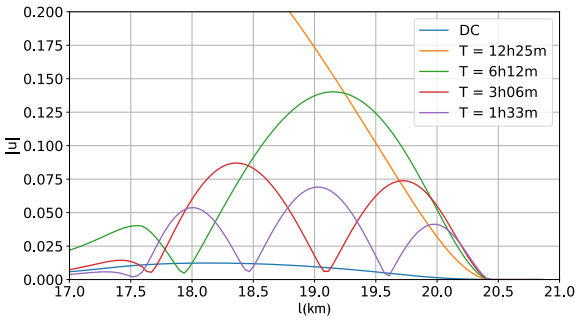

Fig. 4.10 Amplitude of different frequencies for $u(x,t)$ zoomed in at the end of the basin.

Since it would not be clear/useful to plot the frequency spectrum for every different location, instead the amplitude of the $(0, \frac{1}{2\pi}, \frac{1}{\pi}, ...)$ are plotted in Figures 4.7-4.10. It can be seen that for the depth the DC component is the largest due to the seabed and also decreases towards the coast. For the velocity the forcing frequency, M2 tide, is the largest. At the landward side of the basin (Figures 4.9 and 4.10) the amplitude of the frequencies are much bigger due to the fact that it sometimes dry and sometimes wet due to the moving boundary.

4.2 Parameter variation

For equations (2.16) and boundary condition (2.17) the parameters of the system can vary for different tidal inlet systems. The parameters that can be varied are the gravitational constant g, the angular frequency of the semidiurnal tide ω, the reference height H, the amplitude of the semidiurnal tide A, and the resistance r.

Considering that g and ω practically do not change (unless another planet is visited), these parameters will not be varied.

Therefore the variation in parameters will be for A, L, r and H. When these parameters are varied, it is possible that κ changes. Then attention must be paid to the stability criterion ($\sqrt{\kappa}\frac{\Delta t}{\Delta x} \leq 0.9$). Therefore it might be needed to change Δt to keep the numerical method stable. In Table 4.2 the default (Ameland) parameters are given and how they are varied.

Parameter	Ameland	Increased	Decreased
Amplitude A	0.84m	2m	0.4m
Length L	19km	30km	10km
Height H	12m	24m	5m
Resistance r	0.24	5	0

Table 4.2 Variation of the physical parameters.

In the following sections each parameter is varied and then compared to the default parameter. The default parameter results will be plotted using gray lines for the depth and velocity and

a green line for the basin length.

For all the results the seabed is a straight line, except for the results shown in section 4.2.6. Here the model is used for a concave and a convex seabed.

4.2.1 Length of the basin

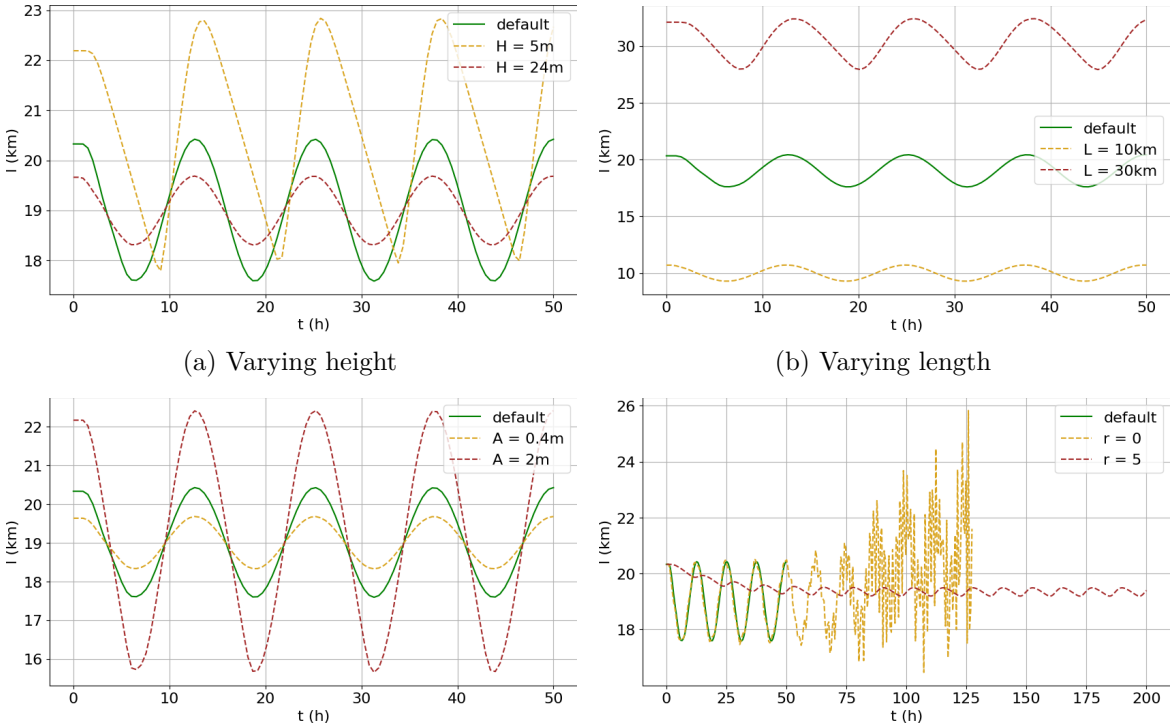

(a) Varying height

(b) Varying length

(c) Varying amplitude

(d) Varying resistance

Fig. 4.11 The length l of the basin as a function of time t for varying parameters.

In Figure 4.11 the length of the basin is plotted for varying parameters. For increasing the amplitude A the basin length $l(t)$ increases. Decreasing H also causes the basin length to increase. For increasing L the basin length $l(t)$ increases partly due to the bigger L. For $r = 0$ the system is unstable and for r increasing the length does not vary much. The systems that are stable, become periodic after 12.5 hours, except for Figure 4.11d. Here the system is stable after 150 hours.

4.2.2 Varying the amplitude

The amplitude of the M2 tide in the Ameland tidal inlet system is $A = 0.84$m. However this amplitude varies at different locations. In Figure 4.12 the depth and velocity are plotted for $A = 0.4$m and a bigger amplitude of $A = 2$m.

The amplitude is present in the boundary condition at $x = 0$, see Eq. (2.17a). This boundary condition is a periodically forced wave. An increase of the amplitude A results in this forcing

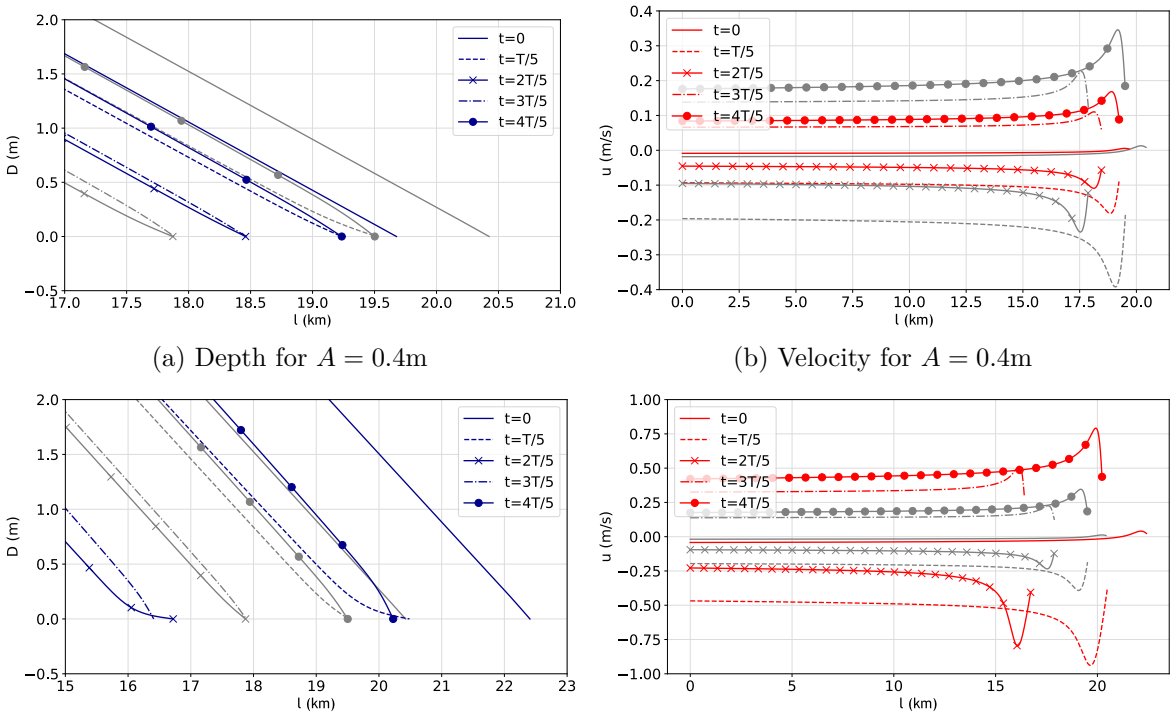

(a) Depth for $A = 0.4$m

(b) Velocity for $A = 0.4$m

(c) Depth for $A = 2$m

(d) Velocity for $A = 2$m

Fig. 4.12 Plot of the $D(x,t)$ (left) and $u(x,t)$ (right) where the amplitude is varied at different times during one period. The grey line represents the default amplitude.

term to be bigger. As can be expected this will then result in a higher velocity and the sea depth being bigger, therefore also increasing the length of the basin. All this can be seen in Figures 4.12d and 4.12c. In Figure 4.12c it is also shown that the non-linearities are more pronounced. For smaller A the opposite happens as shown in Figure 4.12a and 4.12b.

4.2.3 Varying the length

Varying the parameter L causes $\kappa = \dfrac{gH}{(\omega L)^2}$ to change. Therefore it is important to check the stability criterion (3.12) for decreasing L. The characteristic velocity scale U scales with L. Therefore when L increases, the velocity increases. The velocity increase, causes the water to flow farther. Thus it is also expected that the overall depth is increased. This is illustrated in Figure 4.13. In Figure 4.11b it can also be seen that the difference between the maximum and minimum length of the basin is bigger.

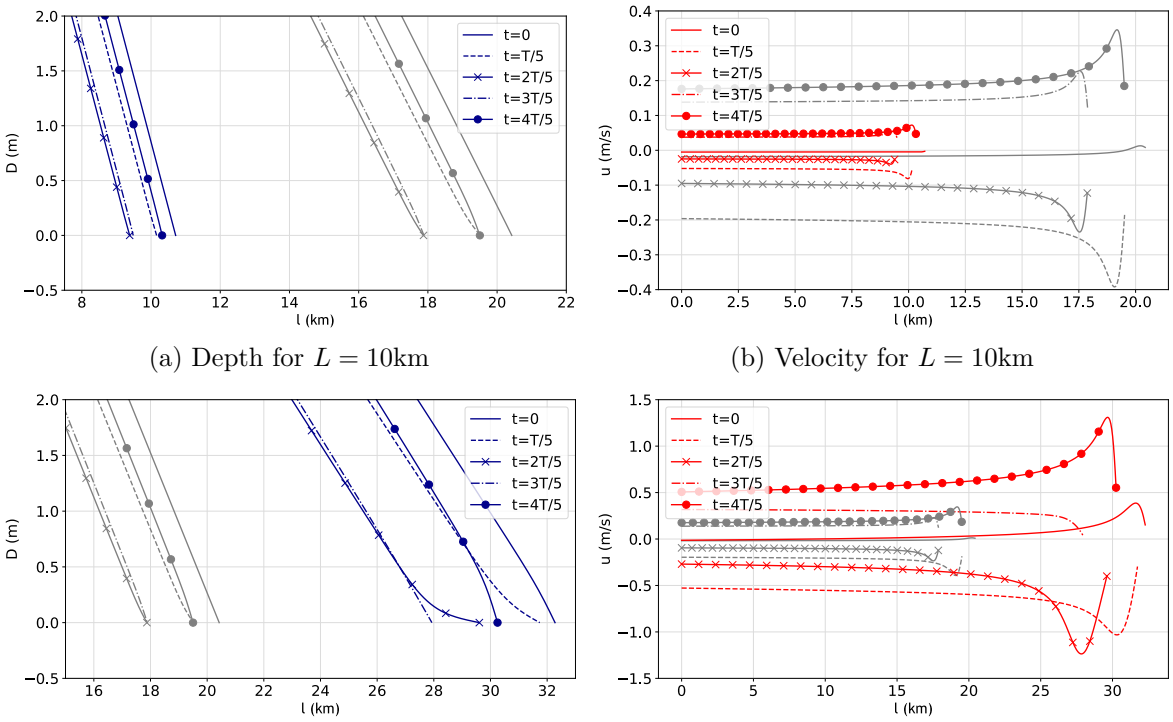

(a) Depth for $L = 10$km

(b) Velocity for $L = 10$km

(c) Depth for $L = 30$km

(d) Velocity for $L = 30$km

Fig. 4.13 Plot of the $D(x,t)$ (left) and $u(x,t)$ (right) where the length is varied at different times during one period. The grey line represents the default length.

4.2.4 Varying the height

If the height H is varied, both the periodic forcing term and $\kappa = \dfrac{gH}{(\omega L)^2}$ change. Increasing H is therefore a combination of decreasing the periodic forcing term (smaller A) and an increased κ (decreased L). Since a smaller A and smaller L have the same results (smaller velocities, smaller length and smaller depth). Therefore an equivalent result is expected when H is increased. This can be seen in Figures 4.14c and 4.14d. Viceversa the opposite can be seen in Figures 4.14a and 4.14b where a decrease in H is similar to an increase of A and increase of L.

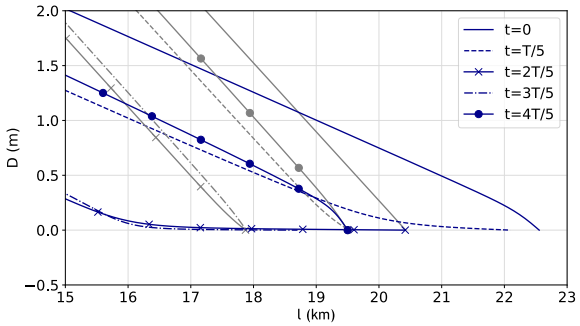

(a) Depth for $H = 5$m

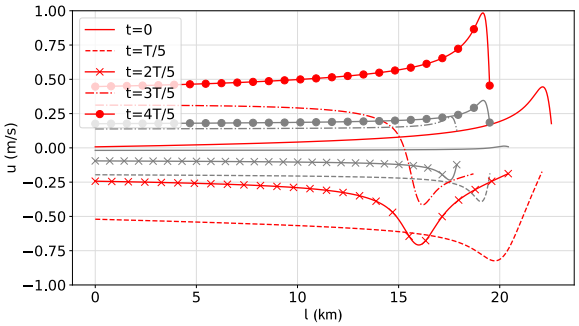

(b) Velocity for $H = 5$m

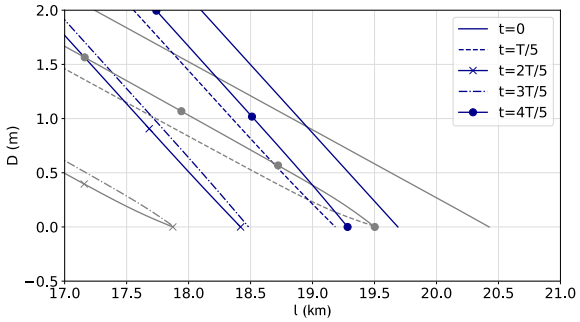

(c) Depth for $H = 24$m

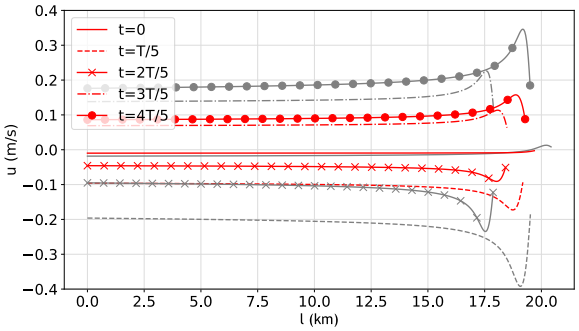

(d) Velocity for $H = 24$m

Fig. 4.14 Plot of the $D(x,t)$ (left) and $u(x,t)$ (right) where the height (the undisturbed water depth) is varied at different times during one period. The grey line represents the default height.

4.2.5 Varying the resistance

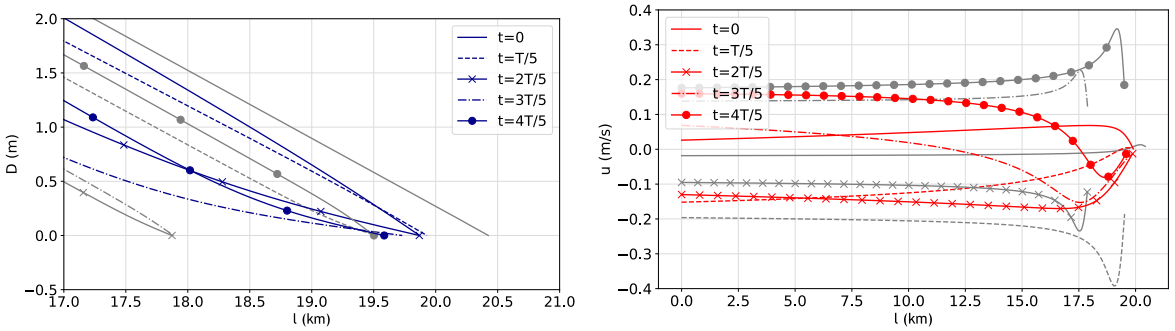

(a) Depth for $r = 5$

(b) Velocity for $r = 5$

Fig. 4.15 Plot of the $D(x,t)$ (left) and $u(x,t)$ (right) where the resistance is varied at different times during one period The grey line represents the default resistance.

The term $\dfrac{ru}{D+h_0}$ represents a negative feedback loop. Therefore $r = 0$ makes the system unstable which was seen in Figure 4.11d. Therefore in Figure 4.15 the (dimensionless) resistance is plotted for $r = 5$ and not for $r = 0$.

Increasing r, causes the resistance term to become vary large (especially at $x = l(t)$). Therefore the resistance is bigger when the water tries to flow back, and therefore the length will not vary as much. Also the negative feedback is bigger, so the velocity has a smaller variation.

4.2.6 Different seabed

In this section, instead of a straight line, a convex and concave seabed is used. In Figure 4.16 the length is plotted. It can be seen that for both seabeds, the length becomes periodically stable.

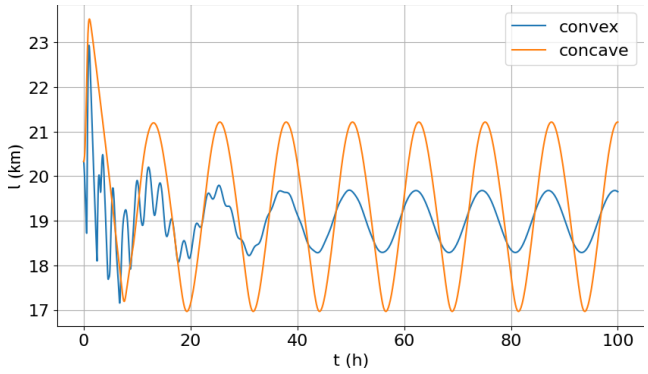

Fig. 4.16 Length of the basin for a concave and convex seabed.

In Figures 4.17 and 4.18 the depth is plotted for convex and concave seabeds. For the concave seabed, the slope at the end of the basin gets flatter and is similar to what happens when L is

increased. For a convex seabed, the slope is actuallty steeper and therefore more similarities to $L = 10$km. This is especially seen in Figures 4.19 and 4.20. The same holds for the velocities (Figures 4.21 and 4.22) where it can be seen that for a concave seabed the velocities are in general much larger.

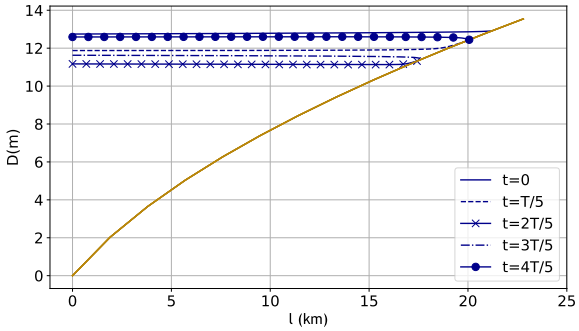

Fig. 4.17 $D(x,t)$ seabed concave.

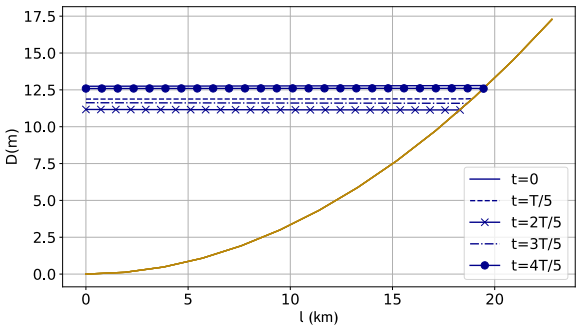

Fig. 4.18 $D(x,t)$ seabed convex.

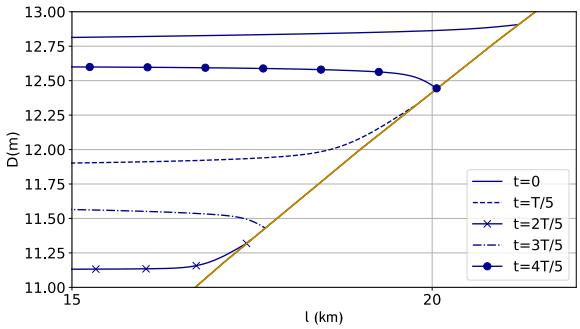

Fig. 4.19 $D(x,t)$ seabed concave zoomed in.

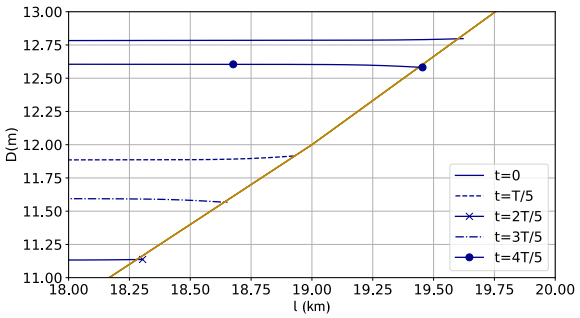

Fig. 4.20 $D(x,t)$ seabed convex zoomed in.

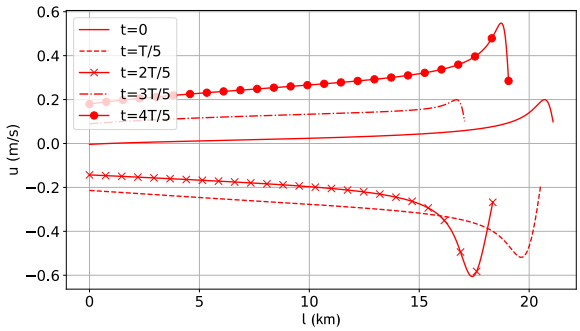

Fig. 4.21 $u(x,t)$ seabed concave.

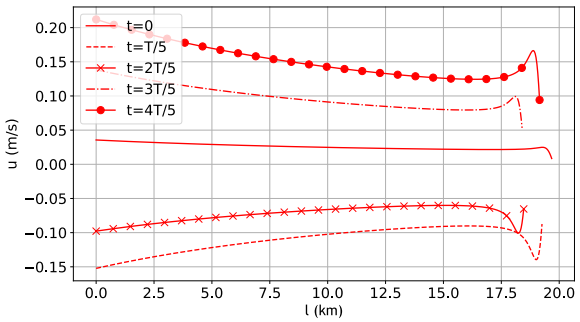

Fig. 4.22 $u(x,t)$ seabed convex.

Fig. 4.23 Combined figures showing different aspects of seabed profiles.

Chapter 5

Conclusion

In this thesis the moving boundary caused by ebb and flood is incorporated into the one dimensional shallow water equations. The 3D shallow water equations are derived from the Navier Stokes equations, which are then cross-sectionally averaged over the depth and width resulting in the 1D shallow water equations.

The 1D shallow water equations are then scaled and transformed by the coordinate transformation $\hat{x} = \frac{x}{l(t)}$ with $l(t)$ the varying length of the inlet. This causes the boundaries to be fixed. However, an extra non-linear term appears in the system of equations and an extra equation is needed for $l(t)$. At the landward side the depth of the sea is 0 and at the seaward side the boundary condition is a periodically forced wave.

To numerically solve the non-linear system of equations, the Lax-Friedrichs method is implemented. The results are then plotted and analyzed for physical parameters of the Ameland tidal inlet system. Then those physcial parameters are varied to analyze the model.

Research questions

It has been shown that the Lax-Friedrichs method is stable under the CFL-condition. This answers *Q1.* A refined grid is needed since the method is highly dispersive. How fine the grid should be depends on the convergence. It was demonstrated that for a certain h_0, the results become independent of spatial and temporal discretization, answering *Q2.*

For the Ameland system the result of the water depth, velocity and length of the basin are plotted. The results are realistic but do still need to be validated *(Q3).* A Fourier Analysis is done, and shows in the frequency spectrum peaks at the periodic forcing frequency and the frequencies of the overtides.

There are 5 different parameters that are varied. If the amplitude of the periodic forced wave or length of the basin is increased, the depth, velocity and length of the system all increase. The opposite happens when the height is increased. If the resistance is 0, the system is unstable. If the resistance is increased, the length of the basin varies more slowly (since it is more difficult for the water to flow back) and the velocity/depth decrease. This answers the

last sub-question *(Q4)*.

The main research question was: *can a coordinate transformation in conjunction with a time-explicit method be used to model the moving boundary problem in shallow waters?*. The four subquestions answered above, motivate that this is indeed the case.

Further research

Although the results are very similar to what is expected, there have been many simplifications. The most obvious one is that it is a one-dimensional model. An improvement would be to extend the model to 3D, and see if the 1D behaviour is still present. Furthermore, the shallow water equations have many simplifications. For example, there are no wind waves, the seabed is constant in time and the effect of sediment transport is not taken into account. These are all things that can be researched.

The numerical method is stable and eventually converges. However, it is not checked against an analytical solution (simply because this solution is not known). Finding another system with non-linearities and a known solution could be a way to check the model. Additionally, although the solution converges for a very refined grid, refining the grid means an increase in computation time. For $M = 2500$ the computation time was 50 hours. A few suggestions to shorten the running time would be: using an adaptive grid method or changing parameter h_0 to see if the solution converges to the same result and if it converges faster.

Lastly, the full stability analysis was outside the scope of this thesis. However this could still be done using for example the Gershgorin circle theorem. The expectation is, though, that the stability will follow the CFL-criterion quite closely.

References

Balzano, A. (1998). Evaluation of methods for numerical simulation of wetting and drying in shallow water flow models. *Coastal Engineering*, 34(1–2):83–107.

Hudson, J. (1998). *Numerical Techniques for Conservation Laws with Source Terms*. PhD thesis, University of Reading.

National Oceanic and Atmospheric Administration (2007). Tidal analysis and predictions.

Press, W. H., Teukolsky, S. A., Vetterling, W. T., and Flannery, B. P. (1995). *Numerical Recipes in C: The Art of Scientific Computing*. Cambridge University Press, Cambridge, UK, 2nd edition.

Rozendaal, M. P. (2019). An idealised morphodynamic model of a tidal inlet and the adjacent sea. Master's thesis, Delft University of Technology, Delft, Netherlands.

Schuttelaars, H., Heemink, A., and Deleersnijder, E., editors (2022). *The Mathematics of Marine Modelling*. Mathematics of Planet Earth. Springer, Cham.

Takeda, H. (1984). Numerical simulation of run-up by variable transformation. *Journal of the Oceanographical Society of Japan*, 40:271–278.

Ter Brake, M. (2010). *Tidal Embayments*. Phd thesis, University of Twente.

Van der Vegt, M. (2006). *Modeling the dynamics of barrier coasts and ebb-tidal deltas*. PhD thesis, University of Utrecht, Utrecht, Netherlands.

Willemsen, P., Hulscher, S., and Vermaas, T. (2015). Methods for analysing morphodynamics of tidal inlets. *Student Undergraduate Research E-journal!*, 1.

Appendix A

Stability analysis

Von Neumann stability

For the stability of the system of equations (2.16) the Von Neumann stability is used. It should be noted that the Von Neumann stability works for linear systems with constant coefficients. In the Eqn. (2.16) this is not the case. Not only is the system non-linear, the coefficients (x) are not constant. This is solved by linearizing the system and 'freezing' the non-constant coefficients.

For the analysis the procedure of Press et al. (1995) (pages 836-839) is followed. Here the difference equations have solutions in the form of eigenmodes: $u_j^n = u_0 \xi^n e^{ik\Delta xj}$. Here k is the wave number. It must be that $|\xi| \leq 1$ for all k else the system is unstable.

Scenarios

Due to the non-linearities and non-constant coefficients the stability is done for simpler scenarios. These simple scenarios do not have a moving boundary. The landward side is modelled as a cliff. Therefore $\frac{\mathrm{d}l}{\mathrm{d}t} = 0$ and the boundary condition at $x = L$ is $u = 0$. The dimensionless equations are then:

$$\begin{cases} \dfrac{\partial D}{\partial t} + \dfrac{\partial}{\partial x}(Du) = 0, & \text{(A.1a)} \\ \dfrac{\partial u}{\partial t} + u\dfrac{\partial u}{\partial x} = -\kappa(\dfrac{\partial D}{\partial x} + \dfrac{\partial h}{\partial x}) - \dfrac{ru}{D + h_0}. & \text{(A.1b)} \end{cases}$$

No resistance and a flat seabed

In the first case there will be no resistance (so $r = 0$) and the seabed will be flat ($h(x) = 0$). This results in the equations:

$$\begin{cases} \dfrac{\partial D}{\partial t} + \dfrac{\partial}{\partial x}(Du) = 0, & \text{(A.2a)} \\ \dfrac{\partial u}{\partial t} + u\dfrac{\partial u}{\partial x} = -\kappa\dfrac{\partial D}{\partial x}. & \text{(A.2b)} \end{cases}$$

The trivial solution is $u = 0, D = c$ with c a constant. Therefore the linearization of the system is done by $u = \hat{v}$ and $D = c + \hat{d}$. The new equations then result in:

$$\begin{cases} \dfrac{\partial \hat{d}}{\partial t} + \dfrac{\partial}{\partial x}(c\hat{v} + \hat{v}\hat{d}) = 0, & \text{(A.3a)} \\ \dfrac{\partial \hat{v}}{\partial t} + \epsilon\hat{v}\dfrac{\partial \hat{v}}{\partial x} = -\kappa(\dfrac{\partial \hat{d}}{\partial x}). & \text{(A.3b)} \end{cases}$$

Taking only the linear terms and dropping the $\hat{}$. results in:

$$\begin{cases} \dfrac{\partial d}{\partial t} + c\dfrac{\partial v}{\partial x} = 0, & \text{(A.4a)} \\ \dfrac{\partial v}{\partial t} = -\kappa\dfrac{\partial d}{\partial x}. & \text{(A.4b)} \end{cases}$$

The numerical Lax-Friedrichs method is implemented. The system then becomes:

$$\begin{cases} \dfrac{d_j^{n+1} - \frac{1}{2}(d_{j+1}^n + d_{j-1}^n)}{\Delta t} + c\dfrac{v_{j+1}^n - v_{j-1}^n}{2\Delta x} = 0, & \text{(A.5a)} \\ \dfrac{v_j^{n+1} - \frac{1}{2}(v_{j+1}^n + v_{j-1}^n)}{\Delta t} = -\kappa\dfrac{d_{j+1}^n - d_{j-1}^n}{2\Delta x} & \text{(A.5b)} \end{cases}$$

The eigenmodes of the Von Neumann stability analysis are used: $d_j^n = d_0\xi^n e^{ik\Delta xj}$ and $v_j^n = v_0\xi^n e^{ik\Delta xj}$. Dividing by $\xi^n e^{ik\Delta xj}$ results in:

$$\begin{cases} d_0\xi = \dfrac{1}{2}(d_0 e^{ik\Delta x)} + d_0 e^{-ik\Delta x}) - \dfrac{c\Delta t}{2\Delta x}(v_0 e^{ik\Delta x} - v_0 e^{-ik\Delta x}), & \text{(A.6a)} \\ v_0\xi = \dfrac{1}{2}(v_0 e^{ik\Delta x} + v_0 e^{-ik\Delta x}) - \dfrac{\kappa\Delta t}{2\Delta x}(d_0 e^{ik\Delta x} - d_0 e^{-ik\Delta x}). & \text{(A.6b)} \end{cases}$$

The resulting matrix equation:

$$\begin{bmatrix} \xi - \cos(k\Delta x) & i\dfrac{c\Delta t}{\Delta x}\sin(k\Delta x) \\ i\dfrac{\kappa\Delta t}{\Delta x}\sin(k\Delta x) & \xi - \cos(k\Delta x) \end{bmatrix} \begin{bmatrix} d_0 \\ v_0 \end{bmatrix} = \begin{bmatrix} 0 \\ 0 \end{bmatrix} \quad \text{(A.7)}$$

Calculating the determinant and setting it equal to 0: $\xi = \cos(k\Delta x) \pm i\dfrac{\sqrt{c\kappa}\Delta t}{\Delta x}\sin(k\Delta x)$

The length of ξ should be ≤ 1 for all wavenumbers k, so

$$|\xi| = \sqrt{1 + \sin^2(k\Delta x)(\frac{c\kappa\Delta t^2}{\Delta x^2} - 1)} \leq 1.$$

In other words: $\dfrac{c\kappa(\Delta t)^2}{(\Delta x)^2} \leq 1$. That is $\Delta t \leq \dfrac{1}{\sqrt{c\kappa}}\Delta x$. By scaling $c = 1$, this is the same as the CFL condition.

Flat seabed

To advance the system, the dimensionless resistance is now set to 0.24. The seabed is still flat. The resulting system of equation is:

$$\begin{cases} \dfrac{\partial D}{\partial t} + \dfrac{\partial}{\partial x}(Du) = 0, & \text{(A.8a)} \\ \dfrac{\partial u}{\partial t} + \epsilon u \dfrac{\partial u}{\partial x} = -\kappa(\dfrac{\partial D}{\partial x}) - \dfrac{ru}{D + h_0}. & \text{(A.8b)} \end{cases}$$

To linearize the system the trivial solutions must be found. These are again $u = 0, D = c$ with c a constant. Therefore use $u = \hat{v}$ and $D = c + \hat{d}$. Then the new system of equations becomes:

$$\begin{cases} \dfrac{\partial \hat{d}}{\partial t} + \dfrac{\partial}{\partial x}(c\hat{v} + \hat{v}\hat{d}) = 0, & \text{(A.9)} \\ \dfrac{\partial \hat{v}}{\partial t} + \epsilon \hat{v} \dfrac{\partial \hat{v}}{\partial x} = -\kappa \dfrac{\partial \hat{d}}{\partial x} - \dfrac{r\hat{v}}{c + \hat{d} + h_0}. & \text{(A.10)} \end{cases}$$

For the nonlinear term of the resistance, a Taylor expansion is used:

$$r\hat{v}\frac{1}{c + \hat{d} + h_0} \approx r\hat{v}(\frac{1}{c + h_0} - \frac{\hat{d}}{(c + h_0)^2}).$$

Taking only the linear terms and dropping the $\hat{}$ results in:

$$\begin{cases} \dfrac{\partial d}{\partial t} + c\dfrac{\partial v}{\partial x} = 0, & \text{(A.11)} \\ \dfrac{\partial v}{\partial t} = -\kappa \dfrac{\partial d}{\partial x} - \dfrac{r}{c + h_0} v. & \text{(A.12)} \end{cases}$$

Again discretizing the system and using the Lax-Friedrichs method:

$$\begin{cases} \dfrac{d_j^{n+1} - \frac{1}{2}(d_{j+1}^n + d_{j-1}^n)}{\Delta t} + c\dfrac{v_{j+1}^n - v_{j-1}^n}{2\Delta x} = 0, & \text{(A.13a)} \\ \dfrac{v_j^{n+1} - \frac{1}{2}(v_{j+1}^n + v_{j-1}^n)}{\Delta t} = -\kappa \dfrac{d_{j+1}^n - d_{j-1}^n}{2\Delta x} - \dfrac{r}{c + h_0} v_j^{n+1}. & \text{(A.13b)} \end{cases}$$

With an implicit scheme for $\dfrac{rv}{c + h_0}$.

The eigenmodes of the Von Neumann stability analysis are used: $d_j^n = d_0 \xi^n e^{ik\Delta x j}$ and $v_j^n = v_0 \xi^n e^{ik\Delta x j}$. Dividing by $\xi^n e^{ik\Delta x j}$ results in:

$$\begin{cases} d_0\xi = \dfrac{1}{2}(d_0 e^{ik\Delta x)} + d_0 e^{-ik\Delta x}) - \dfrac{c\Delta t}{2\Delta x}(v_0 e^{ik\Delta x} - v_0 e^{-ik\Delta x}), & \text{(A.14a)} \\ v_0\xi = \dfrac{1}{2}(v_0 e^{ik\Delta x} + v_0 e^{-ik\Delta x}) - \dfrac{\kappa\Delta t}{2\Delta x}(d_0 e^{ik\Delta x} - d_0 e^{-ik\Delta x}) - \dfrac{\Delta t r v_0 \xi}{c + h_0}. & \text{(A.14b)} \end{cases}$$

Defining $\alpha := \dfrac{r}{c+h_0}$, the resulting matrix equation is:

$$\begin{bmatrix} \xi - \cos(k\Delta x) & i\dfrac{c\Delta t}{\Delta x}\sin(k\Delta x) \\ i\dfrac{\kappa\Delta t}{\Delta x}\sin(k\Delta x) & \xi - \cos(k\Delta x) + \alpha\Delta t\xi \end{bmatrix} \begin{bmatrix} d_0 \\ v_0 \end{bmatrix} = \begin{bmatrix} 0 \\ 0 \end{bmatrix} \tag{A.15}$$

The value of ξ is calculated by setting the determinant to 0 and defining $\beta := \dfrac{c\kappa(\Delta t)^2}{(\Delta x)^2}$:

$$\xi = \frac{(2+\alpha\Delta t)\cos(k\Delta x) \pm \sqrt{\Big(\alpha\Delta t\cos(k\Delta x)\Big)^2 - 4\beta(1+\alpha\Delta t)\sin^2(k\Delta x)}}{2(1+\alpha\Delta t)}. \tag{A.16}$$

For all k, $|\xi|$ must be smaller or equal to 1. Unlike the previous section, this is now done numerically. For different chosen Δx the value of Δt is calculated such that for all k all $|\xi| \leq 1$. The limit ($|\xi| = 1$) is plotted in Figure A.1, the blue line represent the scenario with no resistance (CFL condition) and the orange line represent this scenario. Both scenarios use $c = 1$.

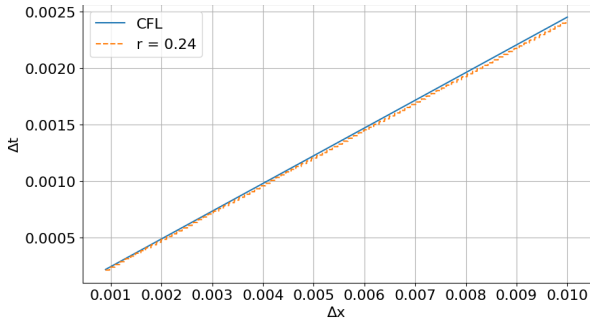

Fig. A.1 For different Δx the value of Δt is plotted when $|\xi| = 1$ (orange line) the blue line is the CFL condition.

Straight line as seabed

For this scenario the seabed is given by $h(x) = 0.9x$. The dimensionless resistance is still $r = 0.24$. The system of equations is:

$$\begin{cases} \dfrac{\partial D}{\partial t} + \dfrac{\partial}{\partial x}(Du) = 0, & \text{(A.17a)} \\ \dfrac{\partial u}{\partial t} + \epsilon u\dfrac{\partial u}{\partial x} = -\kappa\left(\dfrac{\partial D}{\partial x} + 0.9\right) - \dfrac{ru}{D+h_0}. & \text{(A.17b)} \end{cases}$$

The same procedure is followed as in the previous scenarios. The trivial solution is $u = 0$ and $D = -0.9x + 1$. So the linearization by $u = \hat{v}$ and $D = -0.9x + 1 + \hat{d}$. A Taylor expansion of the fraction is done. Then taking only the linear terms result in the system of equations:

$$\begin{cases} \dfrac{\partial d}{\partial t} + \dfrac{\partial v}{\partial x} - 0.9x\dfrac{\partial v}{\partial x} - 0.9v = 0, & \text{(A.18a)} \\ \dfrac{\partial \hat{v}}{\partial t} = -\kappa\dfrac{\partial \hat{d}}{\partial x} - \dfrac{r\hat{v}}{-0.9x + 1 + h_0}, & \text{(A.18b)} \end{cases}$$

where x is seen as a (non constant) coefficient that will be frozen. Then using Lax-Friedrichs as numerical method the result is:

$$\begin{cases} d_j^{n+1} = \dfrac{1}{2}(d_{j+1}^n + d_{j-1}^n) + (0.9x_j - 1)\dfrac{\Delta t}{2\Delta x}(v_{j+1}^n - v_{j-1}^n) + \Delta t 0.9 v_j^n, & \text{(A.19a)} \\ v_j^{n+1} = \dfrac{1}{2}(v_{j+1}^n + v_{j-1}^n) - \dfrac{\kappa\Delta t}{2\Delta x}(d_{j+1}^n - d_{j-1}^n) - \dfrac{\Delta t r v_j^{n+1}}{-0.9x_j + 1 + h_0}. & \text{(A.19b)} \end{cases}$$

Implementing the eigenmodes $d_j^n = d_0\xi^n e^{ik\Delta xj}$, $v_j^n = v_0\xi^n e^{ik\Delta xj}$ and dividing by $\xi^n e^{ik\Delta xj}$ reads:

$$\begin{cases} d_0\xi = d_0\cos(k\Delta x) + i(0.9x_j - 1)\dfrac{\Delta t}{\Delta x}v_0\sin(k\Delta x) + 0.9\Delta t v_0, & \text{(A.20)} \\ v_0\xi = v_0\cos(k\Delta x) - i\dfrac{\kappa\Delta t}{\Delta x}d_0\sin(k\Delta x) - v_0\xi\Delta t\alpha, & \text{(A.21)} \end{cases}$$

where $\alpha(x_j) \coloneqq \dfrac{r}{-0.9x_j + 1 + h_0}$. The resulting matrix equation is:

$$\begin{bmatrix} \xi - \cos(k\Delta x) & i(1 - 0.9x_j)\dfrac{\Delta t}{\Delta x}\sin(k\Delta x) - 0.9\Delta t \\ i\dfrac{\kappa\Delta t}{\Delta x}\sin(k\Delta x) & \xi - \cos(k\Delta x) + \alpha\Delta t\xi \end{bmatrix} \begin{bmatrix} d_0 \\ v_0 \end{bmatrix} = \begin{bmatrix} 0 \\ 0 \end{bmatrix} \quad \text{(A.22)}$$

The solution then is:

$$\xi = \frac{\cos(k\Delta x)(2 + \alpha\Delta t) \pm \sqrt{(\alpha\Delta t\cos(k\Delta x))^2 - (4 + 4\alpha\Delta t)(\beta\sin^2(k\Delta x)^2 + i\gamma\sin(k\Delta x))}}{2 + 2\alpha\Delta t} \quad \text{(A.23)}$$

With $\beta(x_j) \coloneqq (1 - 0.9x_j)\dfrac{\kappa\Delta t^2}{\Delta x^2}$ and $\gamma \coloneqq \dfrac{0.9\Delta t^2\kappa}{\Delta x}$.

The same condition $|\xi| \leq 1$ for every k should hold. However, now there is also a varying x_j. So $|\xi| \leq 1$ for all k and all x_j. With $x_j = j\Delta x$ for $0 \leq j \leq M$.

Here a problem arises. The system of discretized equations (A.19) is experimentally checked to be stable when the CFL condition is However $|\xi| > 1$ for all x_j.

This can be seen by a Taylor expansion around $k\Delta x = 0$ (setting $\cos(k\Delta x) = 1$ and $\sin(k\Delta x) \approx k\Delta x$) and for the square root:

$$\sqrt{(\alpha\Delta t)^2 - \gamma(4 + 4\alpha\Delta t)(i\gamma k\Delta x)} \approx \sqrt{(\alpha\Delta t)^2} - \frac{i\gamma(4 + 4\alpha\Delta t)k\Delta x}{2\sqrt{(\alpha\Delta t)^2}}.$$

For the plus-component of the square root ξ is:

$$\xi_+ = 1 - i\frac{\gamma k \Delta x}{\alpha \Delta t}. \tag{A.24}$$

Therefore the length of ξ_+ is always bigger at $k\Delta x = 0$ for any x_j. This would mean that the system is never stable. However, experimentally it has been shown that the system is stable.

This is showcased in Figures A.2 and A.3 . Here the length of ξ is plotted for a arbitrary x_j with $\Delta x = 0.01$ and $\Delta t = 0.002$ (which have been experimentally be checked to be stable). At $k\Delta x = 0$ it can be seen that $|\xi_+| > 1$. At $k\Delta x = \pi$ the opposite happens and $|\xi_-| > 1$. Therefore taking the maximum of $|\xi_+|$ and $|\xi_-|$ is always unstable.

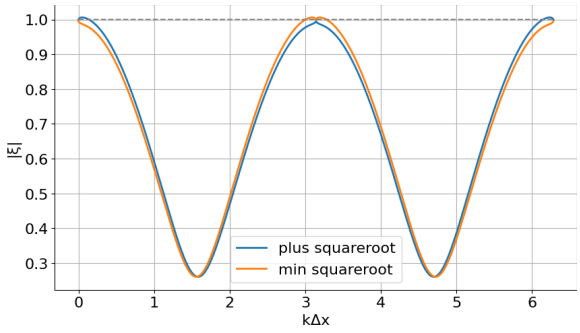

Fig. A.2 Length of ξ plotted for arbitrary x_j.

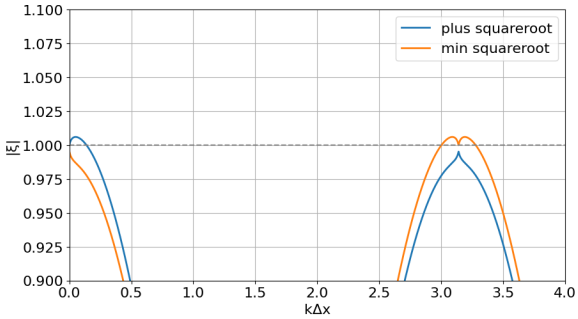

Fig. A.3 Length of ξ plotted for arbitrary x_j zoomed in.

However if the minimum is taken between ξ_+ and ξ_- (which stays below 1), the system again follows the CFL condition as can be seen in Figure A.4.

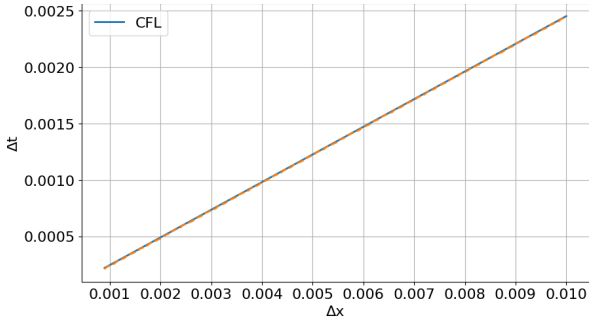

Fig. A.4 For an arbitrary x_j it is checked for different Δx when $|\xi| = 1$. The corresponding Δt is plotted.

From here on the stability analysis is outside the scope of this thesis. However, a motivation for using a restricted CFL conditions has been given. The stability criterion is:

$$\Delta t \leq \frac{0.9}{\sqrt{\kappa}} \Delta x. \tag{A.25}$$